Research Square

Preprints are preliminary reports that have not undergone peer review.
They should not be considered conclusive, used to inform clinical practice,
or referenced by the media as validated information.

Half-graben inversion tectonics revealed by gravity modeling in the Mikawa Bay Region, Central Japan

Ayumu Miyakawa (miyakawa-a@aist.go.jp)
US Geological Survey of Japan, AIST https://orcid.org/0000-0001-8089-6406
Tomoya Abe
Geological Survey of Japan, AIST
Tatsuya Sumita
Geological Survey of Japan, AIST
Makoto Otsubo
Geological Survey of Japan, AIST

Research article

Keywords: Gravity survey, Inversion tectonics, Mikawa Bay Region, Nishi–Mikawa Plain, Chita Peninsula, Utsumi Fault, Takahama Fault, Basement structure, Half-graben, Central Japan, Genetic algorithm

Posted Date: September 15th, 2020

DOI: https://doi.org/10.21203/rs.3.rs-29592/v3

License: This work is licensed under a Creative Commons Attribution 4.0 International License.
Read Full License

Version of Record: A version of this preprint was published on October 20th, 2020. See the published version at https://doi.org/10.1186/s40645-020-00376-6.

Half-graben inversion tectonics revealed by gravity modeling in the Mikawa Bay Region, Central Japan

Ayumu Miyakawa [1]

Corresponding author

Email: miyakawa-a@aist.go.jp

Tomoya Abe [1]

Email: tomoya-abe@aist.go.jp

Tatsuya Sumita [1]

Email: t.sumita@aist.go.jp

Makoto Otsubo [1]

Email: otsubo-m@aist.go.jp

(Institutional addresses)

[1] Geological Survey of Japan, AIST, AIST Tsukuba Central 7, 1-1-1 Higashi, Tsukuba, Ibaraki Pref., 305-8567, Japan

Abstract

The Mikawa Bay Region, central Japan, is characterized by many active faults recording Quaternary activities. It is, however, difficult to understand the overall tectonic character of the region due to a thick sedimentary cover. We report the first finding of Neogene basin inversion in southwest Japan by estimating the depth and structure of the basement surface in the Mikawa Bay Region by analyzing gravity data. Our gravity basement map and two-dimensional density-structure model automatically determined using the genetic algorithm revealed a half-graben bounded on the south by the north-dipping Utsumi Fault. The motion of the Utsumi Fault, which inverted from normal faulting during the Miocene to recent reverse faulting, indicated the inversion of the half-graben. The timing of the inversion of the fault motion, i.e., the reverse faulting of the Miocene normal fault, can be compared with an episode of basin inversion observed at the eastern margin of the Japan Sea, northeastern Japan. The Takahama Fault in the southwestern part of the Nishi–Mikawa Plain is considered to have formed as a result of the backthrust of the Utsumi Fault under inversion tectonics. If the Takahama Fault is indeed the backthrust fault of the Utsumi Fault, the root of the Takahama Fault may be deep such that the Takahama Fault is seismogenic and linked to the 1945 Mikawa earthquake.

Keywords

Gravity survey, Inversion tectonics, Mikawa Bay Region, Nishi–Mikawa Plain, Chita Peninsula, Utsumi Fault, Takahama Fault, Basement structure, Half-graben, Central Japan, Genetic algorithm

Introduction

The Japan Arc is situated in a zone of plate convergence, where crustal activity such as earthquakes is common (Fig. 1 a). Throughout the Japan Arc, there are many faults that are potentially active in the Quaternary. This article is the case in the Mikawa Bay Region, central Japan, close to the Nagoya area, one of Japan's largest urban areas. The evaluation of fault activity is an important issue in Japan; however, it is difficult to understand the overall tectonic characteristics of these active faults due to thick sediments and sea area in the Mikawa Bay Region. The Nishi–Mikawa Plain, also called the Okazaki Plain, a central part of the Mikawa Bay Region, is filled with thick sedimentary rocks and sediments (~1000 m) from the Miocene to Holocene. Quaternary crustal movements of Chita Peninsula, which is surrounded by the sea (i.e., Chita Bay, Mikawa Bay, and Ise Bay), have been well recorded as the elevation distribution of several marine terraces in the Pleistocene (e.g., Makinouchi

1979).

In this study, we focus on the geological structure of the Mikawa Bay Region in order to understand local fault dynamics. Several geological and geophysical studies have been previously undertaken for disaster mitigation in this region. Research conducted by the local government has revealed the basement structure beneath the plain and peninsula (Aichi Prefecture, 2002a, 2002b, 2004, 2005). The top of the basement deepens to the west, although basement rocks are exposed in the eastern area of the plain. The deepest part of the basement lies beneath the Chita Peninsula, where its depth is greater than 1,500 m (Aichi Prefecture, 2002a). Although active faults in the northwest part of the Nishi–Mikawa Plain and the northern part of the Chita Peninsula have been investigated using seismic reflection surveys to image their structures (Aichi Prefecture, 1996), the active faults in the central part of the Nishi–Mikawa Plain and the south part of Chita Peninsula remain under discussion. One such active fault, the Utsumi Fault, runs along the southwestern coast of the Chita Peninsula. Although the Utsumi Fault is expected to play an important role in the formation of the Chita Peninsula, its subsurface structure is poorly known. Furthermore, a comprehensive understanding of the Takahama Fault, which distributes around a large urban area, has yet to be made clear.

In this study, we compiled existing gravity data together with our own gravity measurements

74 in the northern part of the Mikawa Bay Region to image the structure of the basement beneath
75 the Nishi–Mikawa Plain and Chita Peninsula. We revealed the detailed structure including the
76 active faults' orientation using a genetic algorithm (GA) in the central part of the Nishi–
77 Mikawa Plain (i.e., the Takahama Fault) and along the southwestern edge of the Chita
78 Peninsula (i.e., the Utsumi Fault). Then, we discussed the local tectonics with a basin
79 inversion and the conjugate relationship between the Utsumi and Takahama Faults.
80
81 **Study area**
82 The Mikawa Bay Region is located in the southern part of central Japan (Figs. 1 and 2). The
83 Nishi–Mikawa Plain is in the northern Mikawa Bay Region, and the Chita Peninsula is at the
84 west of the Nishi–Mikawa Plain, across Chita Bay. The Nishi–Mikawa Plain is mainly
85 covered with the Pleistocene terraces and alluvial lowland, and its topography is relatively flat
86 (Makimoto et al., 2004). On the other hand, the Chita Peninsula has a relatively high
87 topography. The hills of the Chita Peninsula approximately extend along the N–S trend and
88 primarily consist of the Middle Pleistocene terrace deposits (e.g., the Taketoyo and Noma
89 formations) and Pliocene sedimentary rocks (the Tokai Group), whereas the Miocene
90 sedimentary rocks (the Morozaki Group) are exposed in the southern part of the peninsula
91 (Kondo and Kimura, 1987). The Hazu Mountains and Mikawa Mountains, both of which

92 consist of Mesozoic metamorphic rocks and granite, are located to the southeast and northeast
93 of the Nishi–Mikawa Plain, respectively. The Atsumi Peninsula is elongated in an ENE-WSW
94 direction south of the Nishi–Mikawa Plain across Mikawa Bay. Ise Bay lies at the west of the
95 Chita Peninsula. The largest plain close to this region, the Nobi Plain, is situated to the
96 northwest of the Chita Peninsula.

97 Active faults occur in and around the Nishi–Mikawa Plain and throughout the southern part
98 of the Chita Peninsula (Fig. 2). Long-term evaluations along major active faults in Mikawa
99 Bay Region are reported by the Headquarters for Earthquake Research Promotion (2002;
100 2004). The Sanage–Sakaigawa Fault is a NE–SW trending and the Odaka–Obu Fault is a
101 NNW–SSE trending in the northern Nishi–Mikawa Plain. The Ise-wan Fault is along the
102 northeastern edge of the Chita Peninsula. The Kagiya Fault is NNW–SSE trending in the
103 northern the Chita Peninsula. The active faults in the northwest part of the Nishi–Mikawa
104 Plain and the northern part of the Chita Peninsula such as the Ise-wan Fault (Okada et al.
105 2000) as well as the Odaka–Obu and Kagiya faults (Aichi Prefecture, 1996) have been
106 investigated using seismic reflection surveys to image their structures.

107 In this paper, we focused on the three major active faults in central-west part of Mikawa Bay
108 Region whose structures remain under discussion: the Utsumi, Takahama and Kou faults. The
109 Utsumi Fault trends NW–EW along the steep cliffs of the southern edge of the Chita

Peninsula (Fig. 2). A closed depression suggesting a tectonic relief is recognized along the base of the steep cliffs in submarine topography (Goto, 2013). Uplifting on the NE side of the Utsumi Fault is recorded in subsurface Quaternary sediments discovered *via* shallow seismic reflection surveys (Chujo and Suda, 1971; 1972). This uplifting is believed to have formed the present topography of the southern Chita Peninsula. Gravity surveys around the southern part of the Chita Peninsula indicate a remarkably low Bouguer anomaly, suggesting thick sedimentary rocks and a deep basement surface (Chujo and Suda, 1972). Deep seismic surveys able to image the shape of basement in this region have not yet been conducted. The Takahama Fault is a NW–SE trending active fault in the central Nishi–Mikawa Plain. Topographic features along the fault are, however, ambiguous in its southeastern part but clear in the northwestern part. The southwest-dipping reverse fault was discovered by seismic surveys conducted in the northwest (Aichi Prefecture, 1996). Nonetheless, geophysical surveys, such as seismic surveys, have not yet been conducted in the southeastern part of the fault, with the exception of several boring surveys (e.g., Abe et al., 2019a; 2019b). The Kou Fault, another active one in the research area, is a N–S trending and east-dipping (45°E) reverse fault (Kondo and Kimura, 1987). Although the Kou Fault is thought to have been active at the southern end of the N–S Kagiya fault zone traversing the Chita Peninsula, its slip rate is unknown (The Headquarters for Earthquake Research Promotion, 2004). Some studies

have classified the Kou Fault as estimated active fault which is not directly observed on the ground surface but is inferred from topography (Imaizumi et al., 2018).

The Mikawa earthquake (Mw 6.6) occurred in the Mikawa Bay Region on January 13, 1945, causing more than 2,300 causalities (Iida, 1978). Kikuchi et al. (2003) analyzed seismograms of the Mikawa earthquake and revealed that its source was a NW–SE trending reverse fault with a slight left-slip component. The slip distribution mainly consisted of two asperities: one near the hypocenter and the other, with which the heavily damaged area is well correlated, 10–15 km to the northwest from the hypocenter (Kikuchi et al., 2003). Yamanaka (2004) reanalyzed the slip distribution in the 1945 earthquake using additional seismograms; this revised result also showed a large slip in the northwest part of the fault model. Several other studies concerning the Mikawa earthquake have noted the predominant role of N-S or E-W trending faults (i.e., the Yokosuka and Fukozu faults) in the southeast part of the Nishi–Mikawa Plain and the eastern part of the Mikawa Bay. Ando (1974) interpreted the ground movements as observed geodetically in terms of a N-S striking fault. Takano and Kimata (2009) reexamined the ground deformation caused by the earthquake through removing interseismic deformation and coseismic deformation resulting from the 1944 Tonankai earthquake (Mw 7.9), which occurred ~150 km southwest off the Mikawa Bay Region. The estimated slips in the 1945 earthquake for the Yokosuka and Fukozu faults are 1.4 m and 2.5

146 m, respectively. Sugito and Okada (2004) compiled geomorphic and geologic features of the
147 surface rupture associated with the earthquake, and suggested that nearly pure thrust faulting
148 along the southern N-S trending section was the predominant mode of surface faulting during
149 the earthquake. The two prevailing models (i.e., the NW–SE trending fault and the N-S
150 trending fault) are not consistent, thus the structure of the source fault of the Mikawa
151 earthquake is still under discussion.
152
153 **Datasets**
154 We used publicly available gravity datasets and an additional dataset that we observed across
155 the southeast part of the Takahama fault in the central Nishi–Mikawa Plain. Most of the
156 Mikawa Bay Region is covered by the publicly available datasets (Yamamoto et al., 2011;
157 Geological Survey of Japan, 2013; Gravity Research Group in Southwest Japan, 2001) that
158 we used for our analysis (Fig. 3a). Furthermore, in order to investigate the detailed structure
159 of the southwest part of the Takahama fault, we conducted additional gravity surveys at 57
160 gravity stations (Supple. Table 1) using a Lacoste and Romberg gravimeter (G-304). The
161 network real-time kinematic techniques with the Virtual Reference Station method using
162 Trimble R10 were applied to determine the location of the gravity stations. Bouguer
163 anomalies were calculated with standard corrections (GSJ Gravity Survey Group, 1989) for

164 free-air, Bouguer, terrain and atmosphere, and normal gravity was removed in accordance
165 with the Geodetic Reference System 1980 (GRS80). Terrain corrections were applied for a
166 range of 60 km using the 30-m gridded terrain data compiled by Murata et al. (2018). This
167 30-m gridded terrain data in the study area mainly comprises 5- and 10-m gridded digital
168 elevation map generated by the Geospatial Information Authority of Japan (GSI) and M7000
169 series digital bathymetry data provided by the Marine Information Research Center. The
170 reduction density of 2.3 g/cm^3 was used to obtain the Bouguer anomaly. This reduction
171 density was visually selected using the Nettleton method (Nettleton, 1939) and allows the
172 removal of topographic effects arising from sedimentary rocks exposed in the Chita Peninsula
173 and Nishi–Mikawa Plain (Fig. 3b).

174 We used available elevation data of the basement surface to constrain the basement
175 structure. We collected the elevation data from publicly available sources (Aichi Prefecture
176 2000; 2004; Kuwahara, 1982; Ministry of Land, Infrastructure, Transport and Tourism, 2008;
177 National Research Institute for Earth Science and Disaster Resilience 2019 and Yamada et al.
178 1984) and originally compiled in this study from boring data provide by Aichi Prefecture,
179 Nishio City (Supple. Table 2). We also used geological maps to obtain some locations where
180 the basement exposed to the ground surface (National Institute of Advanced Industrial
181 Science and Technology, 2020b) (Supple. Table 2).

Methods

We estimated the structure of the basement surface (i.e., the thickness of the overlying sediments) in the Mikawa Bay Region by analyzing gravity anomaly data.

Gravity basement analysis

To investigate the structure of the basement surface in the study area, we first estimated the regional trend of the Bouguer anomaly and obtained the optimal density contrast between the sediment/sedimentary rock and the basement rocks. Observed Bouguer anomaly contains mainly two components: regional trend originated by deep/large structure and local effects of the shallow geology. The regional trend of the Bouguer anomaly is caused by the deep/large structure such as subducting slab beneath Japan and/or the Moho structure of the region, and therefore the regional trend is usually observed as long-wavelength components. On the other hand, shallow geological structure such as the distribution of different rock types or sediment thickness, which forms the focus of this study, produces short wavelength Bouguer anomalies. In the study region, rocks can be divided into two types based on density: lower-density sediments/sedimentary rocks, and higher-density basement rocks (i.e., granite and metamorphic rocks). The representative densities of these rock types exposed in this region are ~1.4–2.3 g/cm^3 for sediments/sedimentary rocks and ~2.5–2.9 g/cm^3 for granite and

200 metamorphic rocks, respectively (Schön 2004). Knowing the density contrast between these
201 two types of rocks allows us to estimate the thickness of the sediments/sedimentary rock
202 covering the basement rocks from the residual Bouguer anomaly after the removal of the
203 regional trend.

204 The regional trend of the Bouguer anomaly (long-wavelength components) and its optimal
205 density contrasts are estimated based on the elevation of the basement observed in the
206 borehole or outcrop. The observed Bouguer anomaly (g_{BA}) with suitable terrain correction can
207 be explained as the summation of the regional trend ($g_{regional}$) and local effects
208 (short-wavelength component) ($g_{sediments}$).

209 $$g_{BA} = g_{sediments} + g_{regional}$$

210 The regional trend is assumed to be expressed by the polynomial curved surface as follows:

211 $$g_{regional} = f(x, y|s),$$

212 where x and y are coordinates in the rectangular coordinate system and s is the coefficient of
213 the polynomial curved surface (f). The local effect is assumed to be derived from the density
214 contrast between sediments/sedimentary rocks and basement rocks and the thickness of the
215 sediments/sedimentary rocks. We modeled the effect of the sediments/sedimentary rock cover
216 below sea level using an infinite horizontal plate:

217 $$g_{sediments} = -2\pi G \Delta\rho H,$$

where G is the gravitational constant (6.674×10^{-11} $m^3/kg \cdot s^2$), $\Delta\rho$ is the density contrast between the sediments/sedimentary rocks and the basement rocks, and H is the thickness of the sediments/sedimentary rocks below sea level (i.e., elevation of the basement surface). Here, the equation required to express the observed Bouguer anomaly can be written as follows:

$$g_{BA} = -2\pi G\Delta\rho H + f(x, y|s).$$

We obtained the regional component of the polynomial curved surface together with the optimal density contrast by solving the least squares problem for the basement surface elevation below sea level (H_i) at the boring site (x_i, y_i), and then the observed Bouguer anomaly at the site (g_{BAi}):

$$\sum_{i=1}^{N} [g_{BA\,i} + 2\pi G\Delta\rho H_i - f(x_i, y_i|s)] \rightarrow min,$$

where N is the number of the sites at which the depth of the basement and the Bouguer anomaly is known. Minimizing the least square problem is achieved by finding the least square solution to the following simultaneous equations:

$$\begin{bmatrix} F_1 \\ F_2 \\ \vdots \\ F_N \end{bmatrix} = \begin{bmatrix} A_{11} & A_{12} & \cdots & A_{1M} & H_1 \\ A_{12} & A_{22} & \cdots & A_{2M} & H_2 \\ \vdots & \vdots & \vdots & \vdots & \vdots \\ A_{N1} & A_{N2} & \cdots & A_{NM} & H_N \end{bmatrix} \begin{bmatrix} s_1 \\ s_2 \\ \vdots \\ s_M \\ 2\pi G\Delta\rho \end{bmatrix},$$

where $\mathbf{A}$ is the function of the coordinate (x, y). This formula can be written in $\mathbf{F} = \mathbf{As}$. Then,

234 the solution can be found by $\left(\mathbf{A}^{\mathrm{T}}\mathbf{A}\right)\mathbf{s}=\mathbf{A}^{\mathrm{T}}\mathbf{F}$.

235 We used 85 control points for the known elevation of the basement surface. The elevation
236 of the basement at some control points is higher than sea level. For these points, the effect of
237 basement topography above sea level on the Bouguer anomaly should be eliminated by
238 applying appropriate corrections (free-air, Bouguer, and terrain) to the typical density of
239 basement rock (Fig. 4). Hence, we calculated the gravitational corrections for each point at
240 which the basement surface is above sea level, using a widely accepted reduction density of
241 2.67 g/cm^3 for granitic rocks. We calculated the corrections for the remainder of the points
242 using a reduction density of 2.3 g/cm^3 according to the Nettleton method outlined above.

243 We solved the least square problem by using the 85 control points and setting a 2nd order
244 polynomial curved function for the regional trend of the Bouguer anomaly. We employed the
245 polynomial curved function for the regional trend following that of Makino and Endo (1999)
246 (i.e., $f\left(x,y\,|\,s\right)=s_1x^2y^2+s_2x^2y+s_3x^2+s_4xy^2+s_5xy+s_6x+s_7y^2+s_8y+s_9$), although it is
247 different from the general 2nd order polynomial function. Thereafter, we obtained the optimal
248 density contrast as −0.376 g/cm^3 (i.e., a sediment density of 2.294 g/cm^3) (Fig. 5) with the
249 coefficients of the 2nd order polynomial curved function (Table 1). The obtained optimal
250 density is almost the same as the value set for the sediments/sedimentary rock justified by
251 using the Nettleton method (2.3 g/cm^3). The regional trend of the Bouguer anomaly along the

252 2nd order polynomial curved surface is highest in the southeast region and gradually decreases
253 toward the northwest (Fig. 3c). This regional trend is consistent with results reported in the
254 Aichi Prefecture (2002a). The estimation error at the control points is approximately ± 200 m
255 according to the difference between the observed elevation and the calculated elevation of the
256 basement surface (Fig. 6).
257 Finally, we obtained a map of the basement surface by extracting the regional trend from the
258 observed Bouguer anomaly (Fig. 3d) and multiplying the constants of the infinite horizontal
259 plate (0.0158 $=-2\pi G(-0.376)$ mgal/m) (Fig. 7).
260

261 **Detailed modeling of the basement profile**

262 The estimation of the elevation of the basement surface assumes that the infinite horizontal
263 plate is effective for determining the overall structure but unsuitable for the imaging non-flat
264 structures (e.g., faults and slops). Hence, we conducted additional two-dimensional analysis to
265 model the non-flat structures and to illuminate the detailed structure of the region, including
266 the Utsumi and Takahama faults. We set a SW-NE trending survey line from the southwest of
267 the Chita Peninsula to the central part of the Nishi–Mikawa Plain (Fig. 2b). The initial model
268 was set as the profile of the gravity basement model estimated in the previous step. We then
269 modified the initial model by adding the Utsumi and Takahama faults. Although we also

attempted to model the Kou Fault crossing the survey line, we were unable to constrain the optimal solution because the gravity data lacked sufficient sensitivity on deep and minor structures related to this fault (see details in the Results section). The validity of the model was evaluated by fitting the observed Bouguer anomaly, which is detrended from the regional trend. Gravity stations within 0.5 km onshore and 1.0 km offshore relative to the survey line were used. To select the best fit parameters, we employed the genetic algorithm (GA), a method for solving optimization problems based on a natural selection process that mimics biological evolution (e.g., Goldberg 1989). The method starts from an initial random population, comprising a number of individuals, which are vectors of model parameters, and iteratively improves the estimated solution. At each iteration, fitness to the objective solution is evaluated for each individual gives. The elites, which are fittest individuals, are selected for cross-over to produce offspring that replace the least fit individuals of the current iteration. A small percentage of this new population is arbitrarily mutated, depending on a given mutation rate, so different areas of the search space can be explored. This mutation helps avoid local minima in the optimization process. The new population is also evaluated, allowing only the fittest individuals to survive, and the process is repeated. Therefore, the GA which is able to solve nonlinear global optimization problems is suitable to find the best parameter set in our model.

We obtained the optimal basement model as follows. The synthetic Bouguer anomaly was calculated from the initial model with estimated density contrast (−0.376 g/cm^3) *via* the two-dimensional Talwani's method (Talwani, 1973). Although the overall calculated Bouguer anomaly based on the initial model is consistent with the observed Bouguer anomaly, some discrepancy is observed, especially around the faulted areas (green line in Fig. 8). To reduce these discrepancies, we set parameters to modify the basement structure: the dip of the Utsumi Fault, the dip of the Takahama Fault, the depth shift in the southwest part of the region, the depth shift in the northeast part of the region, the tilt correction of the basement between the Chita Peninsula and Nishi–Mikawa Plain, and the position of the center of tilt correction (see Supple. Figure 1). The dip of the Utsumi Fault in the deep basement is unknown because the depth of the seismic image across the Utsumi Fault is too shallow (~100 m in depth) to capture the shape of the basement (Chujo and Suda, 1971; 1972). Hence, we set the dip of the Utsumi Fault to range from 30°E to 30°W (i.e., 30° to 150° from the east). The dip of the southeast part of the Takahama Fault, through which the survey line passes, is also unknown, although the dip of the northwest part of the fault was estimated to be 70° to 80°W by seismic surveys (Aichi Prefecture, 1996). Hence, we set the dip of the Takahama Fault to range from 30°E to 30°W (i.e., 30° to 150° from the east). The tip (surface position) of the Utsumi and Takahama faults were fixed according to previous studies (Imaizumi et al., 2018; Abe et al.,

306 2019a; 2019b); the tip of the Utsumi Fault was set at 0 km (i.e., with its origin in the
307 horizontal direction), while the tip of the Takahama Fault was set at 22.98 km. Even in the flat
308 basement, the synthetic Bouguer anomaly calculated from the initial model is systematically
309 lower than the observed Bouguer anomaly. Therefore, we set the depth shift in the southwest
310 part (−10–0 km in the horizontal direction) and the northeast part (22.98–30 km in the
311 horizontal direction) to range from −0.2 to 0.2 km and −0.1 to 0.1 km in the vertical direction,
312 respectively. A tilt correction for the basement between the Chita Peninsula and the Nishi–
313 Mikawa Plain ranges from −2° to 2°. The center of the tilt correction ranging from 15 to 18
314 km was also set to provide parameters that fit the lowest Bouguer anomaly observed in the
315 Chita Peninsula.
316 The synthetic Bouguer anomaly at each observation point was calculated by the
317 two-dimensional Talwani's method using a density-structure model with the parameters
318 outlined above. The parameter set which produces the best fit model was searched using the
319 GA (Table 2; Fig. 8 & 9). We set that the elite count and the cross-over fraction were set to
320 5% of the population size and 0.8, respectively. The optimization was terminated when the
321 average change in the fitness value is small enough ($1.0e^{-6}$). To validate the robustness of the
322 GA analysis, we ran the GA 10 times and obtained almost the same results every time, within
323 the range of a few degrees or meters, which is considered sufficient accuracy for the

following discussion (Suppl. Table 3 and Suppl. Fig. 2). We selected the parameter set showing the lowest error from the 10 sets as the optimal parameter set (Table 2).

Results

Basement surface structure around the Nishi–Mikawa Plain

The structure of the basement surface around Mikawa Bay Region is depicted from the Bouguer anomaly (Fig. 7). The basement surface is shallow at the east side of the Nishi–Mikawa Plain, consistent with the exposure of basement rocks in the Mikawa Mountains and Hazu Mountains east of the Nishi–Mikawa Plain. The basement surface deepens from the Nishi–Mikawa Plain to the Chita Peninsula, where its depth is greater than 1,500 m. This trend is consistent with the results of the seismic survey conducted by Aichi Prefecture (2004). The depression of the basement beneath the Chita Peninsula continues to the north of the Nishi–Mikawa Plain.

A NNW–SSE elongated basement high exists in Ise Bay to the west of the northern Chita Peninsula (Fig. 7); we interpret it to be caused by reverse faulting on the Ise-wan Fault that was mapped by Okada et al. (2000). The basement surface becomes considerably shallow toward the west across the Utsumi Fault. Its depth in Ise Bay, far west of Chita Peninsula is, however, inconsistent with results obtained by the seismic reflection survey (Iwabuchi et al.,

342 2000). This area, the Ise Bay far west of Chita Peninsula, is the west edge of our study field,
343 where no boring sites were obtained to control basement surface, thus the regional trend of the
344 estimated Bouguer anomaly might be inappropriate in this region.
345
346 **Fault-related basement surface structure in the Mikawa Bay Region**
347 The depth of the basement surface drastically changes across the Utsumi Fault (Fig. 8). The
348 orientation of the Utsumi Fault indicates a structure like a normal fault that is high dip angle
349 (~70°E) and that the vertical offset of the top-basement horizon is ~2000 m (Fig. 8). The
350 Takahama Fault is a reverse fault with a dip angle of ~60°E (Fig. 8). This dip is consistent
351 with the fault dip observed by seismic-reflection profiling across the northwestern part of the
352 Takahama Fault (Aichi Prefecture, 1996). The gap between the hanging wall is ~200 m,
353 which is relatively smaller than that of the Utsumi Fault. The basement surface tilts and
354 deepens from the Takahama Fault to the Utsumi Fault.
355 We attempted to incorporate the basement surface structure of the Kou Fault by including
356 the Kou Fault with a 45°E dip. It is, however, difficult to constrain the structure arising from
357 the Kou Fault. Even when setting the opposite geometry to that of the basement (i.e., reverse
358 fault and normal fault), both synthetic Bouguer anomalies calculated from the conflicting
359 models are within the range of the observed Bouguer anomaly (Fig. 10). The gravitational

signal from the resulting small, deep structure is dull, such that the signal of the basement surface topography related to the Kou Fault cannot be constrained in our analysis.

Discussion

Inversion tectonics in the Mikawa Bay Region

The topographic features of the basement surface depict a half-graben structure beneath the Chita Peninsula. Depression of the basement surface beneath the Chita Peninsula has been noted in previous studies (Aichi Prefecture, 2002a; 2004; Chujo and Suda, 1972). We found that the Utsumi Fault indicates a normal fault structure with a large gap, and the tilted basement surface forms the hanging wall of the Utsumi Fault (Fig. 8). These structural features correspond to a large half-graben structure in the Mikawa Bay Region, where the Utsumi Fault is the edge fault of the half-graben.

The geometry of the basement surface and uplift forming the Chita Peninsula suggest the inversion tectonics of the half-graben in the Mikawa Bay Region. A discrepancy between the recent reverse faulting and the depressed basement beneath the Chita Peninsula was identified in a previous study (Chujo and Suda, 1972). The recent NE side up reverse faulting (i.e., uplift of the Chita Peninsula side) is recorded in the Quaternary sediments. On the other hand, Miocene normal faulting of the Utsumi Fault is suggested from the thick Miocene sediments

on the hanging wall (Aichi Prefecture, 2005). Therefore, the motion of the Utsumi Fault is shown to have changed from normal faulting in the Miocene to recent reverse faulting (Aichi Prefecture, 2005). This change of motion is interpreted as inversion tectonics related to the half-graben structure discovered herein (Fig. 11).

The lack of knowledge of the geometry of the basement surface by Kou Fault makes it difficult to clarify the role of Kou Fault in the inversion. As shown above, the gravity anomaly could not constrain the structure arising from the Kou Fault. This fact suggests that a displacement of the Kou Fault is less than that of the Utsumi Fault during the inversion process. Therefore, the Kou Fault may be a minor branch fault of the Utsumi Fault, which is the master fault of the inversion. In contrast, the N–S trending Kou Fault is oblique to the NW–SE trending Utsumi Fault. This geometrical discrepancy suggests an irrelevance between the Kou Fault and the Utsumi Fault, and the Kou Fault may have different history to the Utsumi Fault. To conclude the abovementioned issues, more detailed structural exploration is required.

The tectonic history of the Chita Peninsula has been reconstructed using the sediments/sedimentary rocks observed in the region. The thick Miocene sedimentary rocks (Morozaki Group) filled the hanging wall of the Utsumi Fault; hence the motion of the Utsumi Fault was normal in the Miocene (Aichi Prefecture, 2005). The half-graben structure

396 was formed during this extensional stage. Subsequently, Pliocene sedimentary rocks (Tokai
397 Group) were folded with the axis of WNW-ESE before the Middle Pleistocene (Makinouchi,
398 2019). This may suggest that the region was under moderate NNE-SSW compressional stress
399 at this time, which also accounts for the fact that the Utsumi Fault which trends NW–SE was
400 hardly reactivated during this stage. The Utsumi Fault reactivated as a reverse fault around 0.5
401 Ma (following the depositional age of the Middle Pleistocene Taketoyo Formation)
402 (Makinouchi, 2019). The displacement of the reverse faulting was, however, insufficient to
403 recover the gap formed during normal faulting in the Miocene.
404 The tectonic history of the inversion structure in the Chita Peninsula is comparable to
405 inversion tectonics at the eastern margin of the Japan Sea in northeast Japan. The inversion
406 structures in the eastern margin of the Japan Sea are the most completely described inversion
407 structures in Japan (e.g., Okamura et al., 1995; Morijiri, 1996). Normal faults were formed
408 during the Early to Middle Miocene, and were reactivated in the Pliocene to Quaternary
409 (Okamura et al., 1995). Periods of normal fault formation and reactivation in the eastern
410 margin of Japan Sea in northeast Japan coincide with those in the Chita Peninsula. This
411 episode of Miocene normal faulting is believed to be related to the opening of the Japan Sea,
412 whereas the reactivation of reverse faulting motion is considered to be due to E-W
413 compression resulting from the present tectonic setting. Although the tectonic history between

414 central and northeast Japan differs after the opening of the Japan Sea (e.g., Hayashida et al.,
415 1991; Jolivet et al., 1995; Lallemand and Jolivet, 1986; Otofuji et al., 1985), the deduced
416 agreement in the period of the inversion tectonics can be considered a clue to understanding
417 the tectonic dynamics of the Japan Arc.

418 In particular, the onset of positive tectonic inversion in Chita (~0.5 Ma) is significantly
419 younger than that in NE Japan (3–5 Ma). However, the period of normal faulting is the same
420 between both the regions. Previous active fault studies also suggest that the onset of the
421 present tectonic settings and the onset of present active faulting are early in NE Japan and late
422 in SW Japan (e.g., Doke et al. 2012; Miyakawa and Otsubo 2017). This difference in the onset
423 of the positive tectonic inversion and the active faulting could yield a new finding.

424

425 **The Takahama Fault under inversion tectonics**

426 Our results also enable us to discuss the role of the Takahama Fault in the inversion tectonic
427 system in the Mikawa Bay Region. The Takahama Fault constitutes the NE edge of the
428 half-graben (Figs. 8 and 9). Its basement surface is tilted from the Takahama Fault to the
429 Utsumi Fault, although the basement surface is almost flat northeast of the Takahama Fault.
430 Concurrently, the dip orientation of the Takahama Fault is west dipping. Consequently, the
431 Takahama Fault is a “backthrust” of the Utsumi Fault (east dipping). The backthrusts are well

observed in analog inversion tectonics experiments (McClay and Buchanan, 1992) (Fig. 11a). Furthermore, fault traces of both the Takahama and Utsumi Fault observed on the ground surface are NW–SE trending, and both traces are parallel. Such parallel master normal fault and backthrust relationships are observed in three-dimensional analog models reconstructing inversion tectonics (Yamada and McClay, 2004). These geometrical features suggest that the Takahama Fault is a backthrust of the Utsumi Fault, which is the master normal fault of the inversion structure.

The initiation of the reverse faulting period of the Takahama Fault also suggests a conjugate relationship with the reverse faulting of the Utsumi Fault. The initiation/acceleration period of the reverse faulting of the Takahama Fault is estimated to be late Middle Pleistocene base on the analysis of boring cores around the southeastern part of the fault (Abe et al. 2019a; 2019b). This period is a similar one as that of the initiation of reverse faulting of the Utsumi Fault implied from the formation of the Chita Peninsula in late Middle Pleistocene (Makinouchi, 2019). The simultaneity of the initiation of reverse faulting suggests that the Takahama and Utsumi faults are parts of the same inversion tectonic system.

The deep extent of the Takahama Fault within the basement rock cannot be detected by the present gravity survey. However, if the Takahama Fault is the backthrust of the Utsumi Fault, it should reach seismogenic depths. The slip distribution of the 1945 Mikawa earthquake

450 estimated by waveform inversions shows a large slip asperity on the NW–SE trending reverse
451 fault (Kikuchi et al., 2003; Yamanaka, 2004). The location of the northwestern asperity is
452 notably correlated with the heavily damaged area, consistent with the deeper extension of the
453 Takahama Fault (~10 km depth). The strike of the Takahama Fault (N45°W) is parallel to the
454 fault model of the 1945 Mikawa earthquake described by Kikuchi et al. (2003); moreover, the
455 tips of the fault traces are significantly correlated (see, Fig. 2). This agreement suggest that
456 the deep extension of the Takahama Fault can explain the fault model of the northwestern
457 asperity described in Kikuchi et al. (2003) and Yamanaka (2004). The dip of the fault model
458 (30°W) in these studies is, however, lower than the dip estimated in this study (~60°W). This
459 discrepancy may be solved by assuming listric fault geometry in the deeper portion of the
460 Takahama Fault. Based on the leveling data collected by the local government, the 40-cm
461 subsidence of the footwall side (NE side) relative to the hanging wall side along the
462 Takahama Fault in the 1945 Mikawa earthquake (Iida and Sakabe, 1972) supports evidence
463 for reverse faulting of the Takahama Fault during the earthquake. On the other hand, several
464 studies suggest that the N-S trending reverse faults in the southwestward of the Nishi–
465 Mikawa Plain (i.e., the Yokosuka and Fukouzu Faults) were predominant factors in surface
466 faulting during the earthquake (e.g., Ando 1974, Sugito and Okada, 2004; Takano and Kimata,
467 2009). Although remarkable fractures appear on the ground surface along the Yokosuka and

Fukouzu faults where the basement rock is shallow or exposed, the thick and soft Quaternary sediment and Miocene to Pliocene sedimentary rocks covering the Takahama Fault (Aichi Pref 2002a, 2002b, 2004, 2005) may reduce the ground deformation along the Takahama Fault. Therefore, the deep extension of the Takahama Fault, the back thrust of the Utsumi Fault, may be one possible source fault for the 1945 Mikawa earthquake, but this remains difficult to conclude unambiguously.

Conclusions

We analyzed gravity data to describe the basement surface structure in the Mikawa Bay Region. The gravity basement map showed the deepening of the basement surface from the Nishi–Mikawa Plain to the Chita Peninsula. Two-dimensional modeling constrained the orientation of the Utsumi and Takahama faults, although the basement surface structure related to the Kou Fault is so minor that the gravity data cannot constrain it. The basement surface structure from the Nishi–Mikawa Plain to the Chita Peninsula revealed a half-graben structure defined by the Utsumi Fault. The inverse motion of the Utsumi Fault, which underwent normal faulting during the Miocene and recent reverse faulting, is interpreted in

terms of the inversion tectonics of the half-graben. These inversion tectonics, reflecting the reverse faulting of the Miocene normal fault, are comparable to the basin inversion observed at the eastern margin of the Japan Sea in northeastern Japan. The Takahama Fault in the southwestern part of the Nishi–Mikawa Plain is considered to have formed during the backthrust of the Utsumi Fault under inversion tectonics. If the Takahama Fault is indeed the backthrust fault of the Utsumi Fault, the root of the Takahama Fault may be so deep as to reach the seismogenic zone, suggesting that the Takahama Fault may be the source fault of the 1945 Mikawa earthquake.

Abbreviations

GA: Genetic algorithm

Declarations

Availability of data and material

The dataset supporting the conclusions of this article is included within the article and its additional file. Some datasets is available in the cited database in the article.

Competing interests

The authors declare that they have no competing interest.

Funding

(not applicable)

Authors' contributions

AM conducted the gravity observation, analysis and designed the study. TA proposed the topic and supported to compile related information. TS proposed the plan of the analysis and supported the analysis. MO collaborated with the corresponding author in the construction of manuscript. All authors read and approved the final manuscript.

Acknowledgements

We are grateful to T. Komatsubara, T. Sato, S. Okuma and R. Nakashima (Geological survey of Japan, AIST) for their support for our project. The GNSS data were analyzed by Y. Takahashi, who is the staffs of Geological Survey of Japan, AIST. Prof. H. Hoshi (Aichi University of Education) gives us impressive comments. Some figures were generated using

Generic Mapping Tools (Wessel et al., 2013). We appreciate Aichi Prefecture and Nishio City offering their boring data. Constructive comments from the editor, Yo Fukushima, and journal reviewers, Yasutaka Ikeda and an anonymous reviewer, are greatly appreciated.

References

Abe T, Nakashima R, Naya T (2019a) Reports of coring survey in Aburagafuchi Lowland, southwestern part of Nishimikawa Plain, central Japan. GSJ Interim Report 79: 71–86. (in Japanese with English abstract) https://www.gsj.jp/data/coastal-geology/GSJ_INTERIMREP_079_2019_07.pdf

Abe T, Nakashima R, Naya T, Mizuno K (2019b) Subsurface geology along the Takahama Fault in the southwestern part of the Nishimikawa Plain. Annual Meeting of the Association of Japanese Geographers, Autumn 2019, The Association of Japanese Geographers. (in Japanese) https://doi.org/10.14866/ajg.2019a.0_172

Aichi Prefecture (1996) Report of the research on the active faults in the North Chita and the East Kinuura Areas. (in Japanese).

Aichi Prefecture (2000) Underground structure in the Nobi plain (in Japanese). http://www.hp1039.jishin.go.jp/kozo/Aichi6Cfrm.htm (Accessed 14 Aug 2020)

Aichi Prefecture (2002a) Subsurface Survey Report of Sedimentary Basin under the Mikawa Plain. Aichi Prefecture in 2001, Nagoya. (in Japanese) http://www.hp1039.jishin.go.jp/kozo/Aichi6Bfrm.htm (Accessed 14 Aug 2020)

Aichi Prefecture (2002b) Subsurface Survey Report of Sedimentary Basin under the Mikawa Plain. Aichi Prefecture in 2002, Nagoya. (in Japanese) http://www.hp1039.jishin.go.jp/kozo/Aichi7Bfrm.htm (Accessed 14 Aug 2020)

Aichi Prefecture (2004) Subsurface Survey Report of Sedimentary Basin under the Mikawa Plain. Aichi Prefecture in 2003, Nagoya. (in Japanese) http://www.hp1039.jishin.go.jp/kozo/Aichi8frm.htm (Accessed 14 Aug 2020)

Aichi Prefecture (2005) Subsurface Survey Report of Sedimentary Basin under the Mikawa Plain. Aichi Prefecture in 2004, Nagoya. (in Japanese) http://www.hp1039.jishin.go.jp/kozo/Aichi9Bfrm.htm (Accessed 14 Aug 2020)

Ando M (1974) Faulting in the Mikawa earthquake of 1945. Tectonophysics 22(1–2):173–186. https://doi.org/10.1016/0040-1951(74)90040-7

Chujo J, Suda Y (1971) Gravitational survey of northern Ise Bay. Bull Geol Surv Jpn 22(8):415–435. (in Japanese with English abstract) https://www.gsj.jp/data/bull-gsj/22-08_02.pdf

Chujo J, Suda Y (1972) Gravitational survey of southern Ise Bay and Mikawa Bay. Bull Geol Surv Jpn 23(10):573–594. (in Japanese with English abstract) https://www.gsj.jp/data/bull-gsj/23-10_01.pdf

Doke R, Tanikawa S, Yasue K, Nakayasu A, Niizato T, Umeda K, Tanaka T (2012) Spatial patterns of initiation ages of active faulting in the Japanese Islands. Active Fault Research 37, 1–15 (in Japanese with English abstract). https://doi.org/10.11462/afr.2012.37_1

Geological Survey of Japan (2013) Gravity Database of Japan. DVD edition, Digital Geoscience Map P-2. Geological Survey of Japan, AIST, Tsukuba.

576

577 Goldberg DE (1989) Genetic algorithms in search, optimization, and machine learning.
578 Addison-Wesley, Boston.

579

580 Goto H (2013) Submarine anaglyph images around Japan Islands based on bathymetric
581 charts: Explanatory text and sheet maps. Hiroshima Univ Stud Grad Sch Lett 72:1–74, (In
582 Japanese with English abstract). http://doi.org/10.15027/35603

583

584 Gravity Research Group in Southwest Japan (2001) Gravity database of Southwest Japan
585 (CD-ROM). Bull Nagoya University Museum, Special Report No. 9, Nagoya University
586 Museum, Nagoya.

587

588 GSJ Gravity Survey Group (1989) On the standard procedure SPECG1988 for evaluating the
589 correction of gravity at the Geological Survey of Japan. Bull Geol Surv Jpn 40(11):601–
590 611. (in Japanese with English abstract) https://www.gsj.jp/data/bull-gsj/40-11_02.pdf

591

592 Hayashida A, Fukui T, Torii M (1991) Paleomagnetism of the Early Miocene Kani Group in
593 southwest Japan and its implication for the opening of the Japan Sea. Geophys Res Lett

18(6):1095–1098. https://doi.org/10.1029/91GL01349

Headquarters for Earthquake Research Promotion (2002) Long-term evaluation of earthquake along the Ise-wan active fault zone. (in Japanese) https://www.jishin.go.jp/regional_seismicity/rs_katsudanso/f097_isewan/ (Accessed 13 Aug 2020)

Headquarters for Earthquake Research Promotion (2004) Long-term evaluation of earthquake along the Byobu-yama and Ena-san active fault zone and Sanage-yama active fault zone. (in Japanese) https://www.jishin.go.jp/regional_seismicity/rs_katsudanso/f053_054_byobu_ena_sanage/ (Accessed 24 Apr 2020)

Iida K (1978) Distribution of the Earthquake damage and Seismic Intensity caused by the Mikawa earthquake of January 13, 1945. Report of the Earthquake Section of Disaster Prevention Committee of Aichi Prefecture. Aichi Prefecture, Nagoya. (in Japanese)

Iida K, Sakabe K (1972) The extension of the Fukozu fault associated with the Mikawa

612 earthquake in 1945. Zisin, 24, 44-55. (in Japanese with English abstract)
613 https://doi.org/10.4294/zisin1948.25.1_44
614
615 Imaizumi T, Miyauchi T, Tsutsumi H, Nakata T (2018) Digital active fault map of Japan
616 [Revised Edition]. University of Tokyo Press, Tokyo. (in Japanese)
617
618 Iwabuchi Y, Nishikawa H, Noda N, Kawajiri C, Nakagawa M, Aoto S, Kato I, Amma K,
619 Nagata S, Kadoya M (2000) Active faults surveys in the Ise Bay. Rep Hydrogr Res 36:73–
620 96. (in Japanese with English abstract)
621 https://www1.kaiho.mlit.go.jp/GIJUTSUKOKUSAI/KENKYU/report/rhr36/rhr36-05.pdf
622
623 Jolivet L, Shibuya H, Fournier M (1995) Paleomagnetic rotations and the Japan Sea opening.
624 In: Taylor B, Natland J (eds) Active margins and marginal basins of the western Pacific.
625 Geophysical Monograph Series, vol 88. American Geophysical Union, Washington, D. C.,
626 pp 355–369. https://doi.org/10.1029/GM088p0355
627
628 Kikuchi M, Nakamura M, Yoshikawa K (2003) Source rupture processes of the 1944
629 Tonankai earthquake and the 1945 Mikawa earthquake derived from low-gain

630 seismograms. Earth Planets Space 55(4):159–172. https://doi.org/10.1186/BF03351745

631

632 Kondo Y, Kimura I (1987) Geology of the Morozaki district. With Geological Map of Japan
633 1:50,000, Morozaki. Geological Survey of Japan, Tsukuba. (in Japanese with English
634 abstract)

635

636 Kuwahara T (1982) Subsurface geology and ground subsidence in Nishimikawa Region (Old
637 Yahagi river drainage basin). Reports on survey, research and countermeasure for ground
638 subsidence 8: 95–136, Environmental Department of Aichi Prefecture. (in Japanese)

639

640 Lallemand S, Jolivet L (1986) Japan Sea: a pull-apart basin? Earth Planet Sci Lett 76(3–
641 4):375–389. https://doi.org/10.1016/0012-821X(86)90088-9

642

643 Makimoto H, Yamada N, Mizuno K, Takada A, Komazawa M, Sudo S (2004) Geological Map
644 of Japan 1:200,000, Toyohashi and Irago Misaki. Geological Survey of Japan, Tsukuba.
645 (in Japanese with English abstract)

646

647 Makino, M, Endo, S (1999). Gravity survey around the area of the Hariharagawa debris flow

at Izumi, Kagoshima Prefecture. Butsuri-Tansa, 52, 153-160. (in Japanese with English abstract)

Makinouchi T (1979) Chita Movements, the tectonic movements preceding the Quaternary Rokko and Sanage Movements. Memoirs of the Faculity of Science, Kyoto University, Series of Geology and Mineralogy, 46 、 61-106. https://repository.kulib.kyoto-u.ac.jp/dspace/handle/2433/186632

Makinouchi T (2019) Active faults in Chita Peninsula and large earthquakes in the Nankai Trough. Chita Peninsula: its history and present 23:1–20. (in Japanese) http://id.nii.ac.jp/1274/00003183/ (Accessed 24 Apr 2020)

McClay KR, Buchanan PG (1992) Thrust faults in inverted extensional basins. In: McClay KR (ed) Thrust tectonics. Springer, Dordrecht, pp 93–104. https://doi.org/10.1007/978-94-011-3066-0_8

Ministry of Land, Infrastructure, Transport and Tourism (2008): Kunijiban, http://www.kunijiban.pwri.go.jp/ (Accessed 9 Sep 2020)

666

667 Miyakawa A, Otsubo M (2017) Evolution of crustal deformation in the northeast–central
668 Japanese island arc: Insights from fault activity. Island Arc. 26(2), e12179.
669 https://doi.org/10.1111/iar.12179

670

671 Morijiri R (1996) Subsurface structure of the southeastern margin of the Japan Sea inferred
672 from Bouguer gravity anomalies. Zishin (J Seismol Soc Jpn 2nd ser) 49(3):403–416.
673 https://doi.org/10.4294/zisin1948.49.3_403 (in Japanese with English abstract)

674

675 Murata Y, Miyakawa A, Komazawa M, Nawa K, Okuma S, Joshima M, Nishimura K,
676 Kishimoto K, Miyazaki T, Shichi R, Honda R, Sawada A (2018) Gravity Map of
677 Kanazawa District, Gravity Map Series (Bouguer Anomalies) 33. Geological Survey of
678 Japan, AIST, Tsukuba. (in Japanese with English abstract)
679 https://www.gsj.jp/Map/EN/geophysics.html (Accessed 24 Apr 2020)

680

681 National Institute of Advanced Industrial Science and Technology (2020a) Active Fault
682 Database of Japan, Research Information Database DB095, National Institute of
683 Advanced Industrial Science and Technology.

https://gbank.gsj.jp/activefault/index_e_gmap.html. (Accessed 22 Apr 2020)

National Institute of Advanced Industrial Science and Technology (2020b) Seamless Digital Geological Map of Japan (1:200,000), https://gbank.gsj.jp/seamless/v2/viewer/?lang=en. (Accessed 28 Apr 2020)

National Research Institute for Earth Science and Disaster Resilience (2019) NIED K-NET, KiK-net, National Research Institute for Earth Science and Disaster Resilience, doi:10.17598/NIED.0004
https://www.kyoshin.bosai.go.jp/kyoshin/db/index_en.html?all%22 (Accessed 9 Sep 2020)

Nettleton LL (1939) Determination of density for reduction of gravimeter observations. Geophys 4(3):176–183.

Okada A, Toyokura I, Makinouchi T, Fujiwara Y, Ito T (2000) The Ise Bay Fault off the Chita Peninsula, Central Japan. J Geogr (Chigaku Zasshi) 109(1):10–26. https://doi.org/10.5026/jgeography.109.10 (in Japanese with English abstract)

Okamura Y, Watanabe M, Morijiri R, Satoh M (1995) Rifting and basin inversion in the eastern margin of the Japan Sea. Isl Arc 4(3):166–181. https://doi.org/10.1111/j.1440-1738.1995.tb00141.x

Otofuji YI, Matsuda T, Nohda S (1985) Opening mode of the Japan Sea inferred from the palaeomagnetism of the Japan Arc. Nature 317(6038):603–604. https://doi.org/10.1038/317603a0

Schön JH (2004) Physical properties of rocks: Fundamentals and principles of petrophysics. Elsevier.

Sugito N, Okada A (2004) Surface rupture associated with the 1945 Mikawa earthquake. Active Fault Res 24:103–127. https://doi.org/10.11462/afr1985.2004.24_103 (in Japanese with English abstract)

Takano K, Kimata F (2009) Re-examination of ground deformation and fault models of the 1945 Mikawa Earthquake (M = 6.8). Zisin (J Seismol Soc Jpn 2nd ser) 62(2+3):85–96.

https://doi.org/10.4294/zisin.62.85 (in Japanese with English abstract)

Talwani M. (1973) Computer usage in the computation of gravity anomalies. Method in Computational Physics, vol 13. Academic Press, New York, pp 343-389. https://doi.org/10.1016/B978-0-12-460813-9.50014-X

Wei D, Seno T (1998) Determination of the Amurian plate motion. In: Flower MFJ Chung SL, Lo CH, Lee TY (eds) Mantle dynamics and plate interactions in East Asia. Geodynamics Series, vol 27. American Geophysical Union, Washington D. C., pp 337–346. https://doi.org/10.1029/GD027p0337

Wessel P, Smith WHF, Scharroo R, Luis J, Wobbe F (2013) Generic mapping tools: Improved version released. EOS Trans AGU 94(45):409–410. doi:10.1002/2013EO450001.

Yamanaka Y (2004) Source rupture processes of the 1944 Tonankai earthquake and the 1945 Mikawa earthquake. The Earth Monthly 26(11):739–745. (in Japanese)

Yamada Y, McClay K (2004) 3-D analog modeling of inversion thrust structures. In: McClay

738 KR (ed) Thrust Tectonics and Hydrocarbon Systems. AAPG Memoir, vol 82. American
739 Association of Petroleum Geologists, Tulsa, pp 276–301.
740 https://doi.org/10.1306/M82813C16

741

742 Yamada T, Takada Y, Yamada N, Asao K, Ohtomo Y (1984) A new fact on the location of the
743 Median Tectonic Line around Cape Irago, Atsumi Peninsula, central Japan. The Journal of
744 the Geological Society of Japan 90(12):915–918. https://doi.org/10.5575/geosoc.90.915
745 (in Japanese)

746

747 Yamamoto A, Shichi R, Kudo T (2011) Gravity database of Japan (CD-ROM). Special
748 Publication No. 1. The Earth Watch Safety Net Research Center, Chubu University,
749 Nagoya.

750

751 ## Figure legends

752 Figure 1. Map showing the tectonic setting of the Japanese islands (a) and the geology of the
753 study area (b) (National Institute of Advanced Industrial Science and Technology 2020b). (a)
754 Thick black lines represent plate boundaries and black arrows represent relative plate motions
755 (after Wei and Seno, 1998). The blue rectangle represents the study area and the green shaded

area is the eastern margin of the Japan Sea (see main text for discussion).

Figure 2. Topography and active faults in the Mikawa Bay Region. Red lines represent the traces of active faults in Figure 1(b) (National Institute of Advanced Industrial Science and Technology, 2020a). The blue line indicates the profile line shown in Figures 8, 9, and 10. The topography is illustrated using the 30 m gridded terrain data compiled by Murata et al. (2018). The top-right panel represents the slip distribution model of the 1945 Mikawa Earthquake (modified after Kikuchi et al., 2003). The increment of contour lines is 0.5 m and the star indicates the epicenter of the 1945 Mikawa Earthquake.

Figure 3. Bouguer anomaly of the study area. (a) Red dots indicate the location of gravity stations used for this analysis. (b) Bouguer anomaly calculated with a reduced density of 2.3 g/cm^3. (c) Regional trend of the Bouguer anomaly. Black dots and crosses represent the boring locations and basement exposing locations, respectively. (d) Residual Bouguer anomaly obtained by deducting the regional trend (c) from the original Bouguer anomaly (b). The topography (a) is illustrated by using the 30 m gridded terrain data compiled by Murata et al. (2018).

774 Figure 4. Schematic diagrams showing the calculation of residual Bouguer anomalies at the
775 boring sites and basement exposure points. (a) Definition of the elevation of points (h) and
776 the density of the basement (ρ_b) and one unit of sediments/sedimentary rocks (ρ_s). The
777 elevation of the buried basement surface is represented by H. (b) Gravitational corrections
778 ($\Delta_{\mathcal{G}}$) (Bouguer, free-air and terrain correction) are calculated using the density of the rock
779 exposed at the observation points. g_n is normal gravity in accordance with the Geodetic
780 Reference System 1980 (GRS80). The corrected Bouguer anomaly (g_{BA}) represents the
781 Bouguer anomaly considered. (c) The residual Bouguer anomaly (g') is obtained by
782 removing the regional trend from the Bouguer anomaly (g_{BA}). The residual Bouguer
783 anomaly must consist of the gravity anomaly from the thickness of the
784 sediments/sedimentary rocks (i.e., the elevation of the basement surface).
785
786 Figure 5. Relationship between the elevation of the basement and the residual Bouguer
787 anomaly at the boring site or basement exposure (Fig. 4). The red line represents the
788 relationship between the elevation of the basement and the residual Bouguer anomaly by
789 using the least square method.
790
791 Figure 6. Difference between the observed elevation of the basement surface and the

792 calculated elevation of the basement surface (see Fig. 5).

793

794 Figure 7. Gravity basement map obtained using the relationship between the depth of the
795 basement and the residual Bouguer anomaly (Fig. 5) based on the the residual Bouguer
796 anomaly map (Fig. 3d).

797

798 Figure 8. Profiles of the Bouguer anomaly (a) and the topography of the basement surface (b).
799 (a) The observed and interpolated residual Bouguer anomalies are represented by the open
800 circles and cyan line, respectively. The interpolated residual Bouguer anomalies come from
801 that of the Fig. 3 (d). The green line and red line represent the calculated Bouguer anomaly
802 from the initial model (green in b) and the optimum model (red in b) using the 2D Talwani's
803 method. (b) The green line represents the initial model extracted from the gravity basement
804 model (Fig. 5) along the survey line. The red line represents the optimum basement model
805 obtained by selecting the best parameters (see Table 2). The black line represents the elevation
806 of the ground surface. The origin of the x-axis is set as the tip of the Utsumi Fault in both a
807 and b.

808

809 Figure 9. Close-up views of the profiles of the Bouguer anomaly (a) and the topography of the

basement surface (b) around the Takahama Fault. The tip of the Takahama Fault is located at 22.98 km. (a) The observed and interpolated residual Bouguer anomalies are represented by open circles and the cyan line, respectively. The interpolated residual Bouguer anomalies come from that of the Fig. 3 (d). The green line and red line represent the calculated Bouguer anomaly from the initial model (green in b) and the optimum model (red in b) using the 2D Talwani's method. (b) The green line represents the initial model extracted from the gravity basement model (Fig. 5) along the survey line. The red line represents the optimum basement model obtained by selecting the best parameters (Table 2). The black line represents the elevation of the ground surface. The origin of the x-axis is set at the tip of the Utsumi Fault in both a and b.

Figure 10. Profiles of the Bouguer anomaly and the topography of the basement surface with 600 m of displacement along the Kou Fault at 2.26 km with a dip of 45°E. (a) Reverse fault structure of the Kou Fault using the optimal basement model. (b) Normal fault structure of the Kou Fault using the optimal basement model. Lines and circles are same as shown in Figure 8. The origin of the x-axis is set at the tip of the Utsumi Fault in both a and b.

Figure 11. (a) Conceptual models for thrust faults developed by the dip-slip inversion of a

normal fault system (modified after McClay and Buchanan, 1992). The white arrow represents normal faulting during the extensional stage. Black arrows indicate reverse faulting during the compressional stage following the extensional stage. (b) Conceptual models for the fault system across the Chita Peninsula and the Nishi–Mikawa Plain (not to scale). The white arrow represents the normal faulting in the extensional stage in Miocene. Black arrows indicate reverse faulting during the compressional stage following extensional stage in the Pliocene to Quaternary.

839 Table 1. Coefficient of the polynomial function representing the regional trend of the Bouguer

840 anomaly.

Table 1. Coefficient of the polynomial function represents the regional trend of Bouguer anomaly								
s_1	s_2	s_3	s_4	s_5	s_6	s_7	s_8	s_9
0.00007	0.00149	-0.02301	-0.00089	0.00083	1.34760	-0.01037	-0.88458	13.61115
The s_i is the coefficient of the following function.								
$f(x, y \mid s) = s_1x^2y^2 + s_2x^2y + s_3x^2 + s_4xy^2 + s_5xy + s_6x + s_7y^2 + s_8y + s_9$								
, wher x and y is local cartesian coordinates (km) from coorindates of an origin 137 °E, 35 °N.								

841

842

843 Table 2. Optimum parameters for the 2D basement model.

Table 2. Optimum parameters for the 2D basement model						
Dip of Utsumi Fault (° E)	Dip of Takahama Fault (° W)	Depth Shift of the basement southweset from the Utsumi Fault (km)	Depth Shift of the basement northeast from the Takahama Fault (km)	Rotation of the basement between the Utsumi and Takahama faults (deg to anticlock wise)	Rotation center of between the Utsumi and Takahama faults (km)	Mean absolute error (mgal)
72.1	61.5	0.095	0.019	1.0	16.886	0.272

844

845

846 Supplementary Table 1. Observed gravity data in the Mikawa Plain, Japan.

Additional Table 1. Observed gravity data in the Mikawa Plain, Japan

No.	Year	Month	Day	Time	Latitude	Longitude	H	Gobs	Gnorm	FAC	BGC	TI	Tw	BGA
1	2018	03	03	0833	345344.3015	1370139.4240	0.813	979742.908	979724.888	1.1208	-0.0342	0.0158	-0.0016	19.0970
2	2018	03	03	0843	345343.5163	1370139.3196	0.835	979742.897	979724.869	1.1276	-0.0352	0.0157	-0.0016	19.1088
3	2018	03	03	0854	345342.6758	1370139.1969	0.862	979742.918	979724.850	1.1359	-0.0363	0.0157	-0.0016	19.1553
4	2018	03	03	0906	345341.7966	1370139.0844	0.864	979742.933	979724.829	1.1365	-0.0364	0.0157	-0.0016	19.1914
5	2018	03	03	0915	345340.9413	1370138.9742	0.805	979742.921	979724.809	1.1183	-0.0339	0.0157	-0.0016	19.1871
6	2018	03	03	0925	345340.0555	1370138.8566	0.749	979742.904	979724.788	1.1011	-0.0316	0.0157	-0.0016	19.1790
7	2018	03	03	0933	345339.1779	1370138.7392	0.704	979742.889	979724.767	1.0872	-0.0297	0.0157	-0.0016	19.1752
8	2018	03	03	0941	345338.3266	1370138.6216	0.694	979742.876	979724.747	1.0841	-0.0292	0.0157	-0.0016	19.1804
9	2018	03	03	0950	345337.4423	1370138.5029	0.656	979742.909	979724.726	1.0724	-0.0276	0.0157	-0.0016	19.2261
10	2018	03	03	1055	345336.5924	1370138.4014	0.586	979742.923	979724.706	1.0508	-0.0247	0.0156	-0.0016	19.2450
11	2018	03	03	1103	345335.7350	1370138.2886	0.650	979742.902	979724.686	1.0705	-0.0274	0.0156	-0.0016	19.2577
12	2018	03	03	1113	345334.8836	1370138.1765	0.602	979742.887	979724.666	1.0557	-0.0254	0.0155	-0.0017	19.2522
13	2018	03	03	1123	345334.6388	1370137.7212	0.742	979742.866	979724.660	1.0989	-0.0313	0.0156	-0.0017	19.2668
14	2018	03	03	1158	345335.1656	1370136.9448	0.731	979742.860	979724.673	1.0955	-0.0308	0.0156	-0.0017	19.2461
15	2018	03	03	1211	345335.0746	1370136.1357	0.627	979742.867	979724.671	1.0634	-0.0264	0.0155	-0.0016	19.2332
16	2018	03	03	1223	345334.4346	1370135.5006	0.584	979742.868	979724.655	1.0502	-0.0246	0.0155	-0.0016	19.2403
17	2018	03	03	1235	345333.8241	1370134.8753	0.622	979742.837	979724.641	1.0619	-0.0262	0.0155	-0.0017	19.2315
18	2018	03	03	1246	345333.1853	1370134.2411	0.541	979742.832	979724.626	1.0369	-0.0228	0.0154	-0.0017	19.2242
19	2018	03	03	1257	345332.5534	1370133.6051	0.662	979742.812	979724.611	1.0742	-0.0279	0.0153	-0.0017	19.2444
20	2018	03	03	1311	345331.9077	1370132.9399	0.776	979742.816	979724.596	1.1094	-0.0327	0.0154	-0.0017	19.2880
21	2018	03	03	1327	345331.2836	1370132.2955	0.793	979742.868	979724.581	1.1146	-0.0334	0.0154	-0.0017	19.3583
22	2018	03	03	1343	345330.6272	1370131.6262	0.776	979742.917	979724.566	1.1094	-0.0327	0.0153	-0.0017	19.4189
23	2018	03	03	1353	345329.9930	1370130.9949	0.833	979742.920	979724.551	1.1270	-0.0351	0.0154	-0.0017	19.4492
24	2018	03	03	1406	345329.3478	1370130.3275	0.887	979742.942	979724.536	1.1436	-0.0374	0.0153	-0.0017	19.4975
25	2018	03	03	1418	345328.7006	1370129.6779	0.884	979742.982	979724.520	1.1427	-0.0372	0.0153	-0.0017	19.5522
26	2018	03	03	1427	345328.0644	1370129.0436	0.943	979743.011	979724.505	1.1609	-0.0397	0.0153	-0.0017	19.6087
27	2018	03	03	1435	345327.4377	1370128.3952	1.004	979743.027	979724.491	1.1797	-0.0423	0.0153	-0.0017	19.6523
28	2018	03	03	1512	345326.7140	1370127.6756	1.119	979743.032	979724.474	1.2152	-0.0471	0.0153	-0.0017	19.6988
29	2018	03	03	1528	345326.0615	1370127.0115	1.166	979743.061	979724.458	1.2297	-0.0491	0.0154	-0.0017	19.7533
30	2018	03	03	1536	345325.4210	1370126.3666	1.223	979743.054	979724.443	1.2473	-0.0515	0.0153	-0.0017	19.7732
31	2018	03	03	1546	345324.8017	1370125.7102	1.270	979743.086	979724.429	1.2618	-0.0535	0.0154	-0.0017	19.8300
32	2018	03	03	1620	345324.1775	1370125.0762	1.336	979743.100	979724.414	1.2822	-0.0563	0.0154	-0.0017	19.8726
33	2018	03	04	0816	345323.5519	1370124.4493	1.342	979743.136	979724.399	1.2840	-0.0565	0.0154	-0.0017	19.9247
34	2018	03	04	0827	345322.9036	1370123.7949	1.401	979743.147	979724.384	1.3022	-0.0590	0.0156	-0.0017	19.9639
35	2018	03	04	0838	345322.2588	1370123.1446	1.477	979743.159	979724.369	1.3257	-0.0622	0.0158	-0.0017	20.0077
36	2018	03	04	0847	345321.6062	1370122.4813	1.529	979743.197	979724.353	1.3417	-0.0644	0.0162	-0.0017	20.0729
37	2018	03	04	0857	345320.9618	1370121.8329	1.672	979743.162	979724.338	1.3858	-0.0704	0.0171	-0.0017	20.0854
38	2018	03	04	0907	345320.3267	1370121.1927	2.069	979743.081	979724.323	1.5083	-0.0872	0.0183	-0.0017	20.1060
39	2018	03	04	0918	345319.0344	1370119.8568	4.636	979742.474	979724.293	2.3002	-0.1953	0.0207	-0.0018	20.0781
40	2018	03	04	0929	345316.7785	1370119.1522	8.877	979741.489	979724.240	3.6086	-0.3739	0.0220	-0.0019	20.0468
41	2018	03	04	0938	345315.7373	1370118.7998	9.401	979741.381	979724.215	3.7702	-0.3960	0.0225	-0.0019	20.0753
42	2018	03	04	1120	345309.1092	1370111.9115	1.953	979743.021	979724.059	1.4725	-0.0823	0.0150	-0.0018	20.2780
43	2018	03	04	1134	345304.9176	1370108.5669	1.800	979742.881	979723.960	1.4253	-0.0758	0.0143	-0.0018	20.2030
44	2018	03	04	1152	345301.4699	1370107.6461	1.649	979742.905	979723.879	1.3787	-0.0695	0.0142	-0.0018	20.2758
45	2018	03	04	1221	345253.5248	1370054.8641	0.916	979742.057	979723.692	1.1526	-0.0386	0.0137	-0.0018	19.4587
46	2018	03	04	1238	345242.0570	1370041.7445	0.904	979741.307	979723.422	1.1489	-0.0381	0.0135	-0.0018	18.9758
47	2018	03	04	1627	345350.3189	1370149.1390	1.570	979743.393	979725.030	1.3544	-0.0661	0.0166	-0.0016	19.6024
48	2018	03	04	1645	345352.1573	1370150.8705	2.395	979743.275	979725.073	1.6089	-0.1009	0.0167	-0.0016	19.6156
49	2018	03	06	1628	345359.0795	1370159.7907	3.961	979743.521	979725.236	2.0920	-0.1669	0.0171	-0.0016	20.0309
50	2018	03	06	1637	345355.4570	1370155.0384	2.097	979743.586	979725.151	1.5169	-0.0883	0.0176	-0.0016	19.7880
51	2018	03	06	1702	345257.6260	1370058.6692	1.300	979742.394	979723.788	1.2711	-0.0548	0.0138	-0.0018	19.7806
52	2018	03	07	0945	345030.7590	1370448.2323	5.439	979750.473	979720.330	2.5479	-0.2291	0.0785	-0.0033	32.3413
53	2018	03	07	1003	345052.8532	1370502.2245	9.259	979750.443	979720.850	3.7264	-0.3900	0.0491	-0.0032	32.5320
54	2018	03	07	1037	344702.7983	1370539.1220	96.056	979729.489	979715.436	30.5029	-4.0431	0.6534	-0.0239	36.7357
55	2018	03	07	1140	344846.6716	1370502.2549	78.979	979732.546	979717.880	25.2348	-3.3248	0.2997	-0.0082	32.9349
56	2018	03	07	1208	344920.5120	1370550.7009	52.508	979739.064	979718.676	17.0687	-2.2109	0.3004	-0.0065	33.0557
57	2018	03	07	1300	345239.7040	1370449.3111	7.477	979752.262	979723.366	3.1767	-0.3149	0.0348	-0.0023	31.4259

Legend

No:	Station Number
Year, Month, Day and Time:	Obsarevation year month day and time in JST (UTC+9)
Latitude:	Latitude (e.g. 242259.9753 means 24 degrees 22 minutes 59.9753 seconds North)
Longitude:	Longitude (e.g. 1241000.4210 means 124 degrees 10 minutes 00.4210 seconds East)
H:	Observation Point Height (m)
Gobs:	Observed gravity value (mGal)
Gnorm:	Normal gravity value (mGal)
FAC:	Free-air correction value (mGal)
BGC:	Bouguer correction value (mGal / 1.0 g/cm^3)
TI:	Terrain correction value (mGal / 1.0 g/cm^3)
Tw:	Sea water correction value (mGal / 1.0 g/cm^3)
BGA:	Bouguer anomaly (assumed density: 2.30 g/cm^3)

Bouguer Anomaly value can be calculated as

$$BGA = Gobs - Gnorm + FAC + (BGC + TI) \times \rho + Tw \times \rho_w$$

where ρ and ρ_w are the assumed densities of surficial rocks and sea water, respectively.

847

848 Supplementary Table 2. Elevation of the basement surface compiled in this study.

Additional Table 2. Elevation of basement top newly compiled in this study						
ID	Longitude (° E)	Latitude (° N)	Basement depth from ground surface (m)	Elevation of ground surface (m)	Elevation of basement top (m)	Source
A1	137.06	34.85	82.8	3.3	-79.5	Aichi Pref.
A2	137.08	34.79	54.7	1.2	-53.5	Nishio City
A3	137.07	34.80	49.1	1.6	-47.5	Nishio City
A4	137.07	34.82	43.5	1.4	-42.1	Aichi Pref.
A5	137.07	34.82	42.0	1.3	-40.7	Nishio City
A6	137.10	34.90	46.6	10.2	-36.4	Aichi Pref.
A7	137.08	34.81	37.8	2.8	-35.0	Nishio City
A8	137.08	34.82	33.6	0.8	-32.8	Nishio City
A9	137.08	34.82	36.9	4.3	-32.6	Nishio City
A10	137.10	34.90	43.1	10.6	-32.5	Aichi Pref.
A11	137.08	34.86	31.9	4.9	-27.0	Nishio City
A12	137.08	34.86	31.9	4.9	-27.0	Nishio City
A13	137.10	34.86	32.0	5.2	-26.8	Aichi Pref.
A14	137.10	34.86	31.4	5.5	-25.9	Nishio City
A15	137.10	34.86	31.4	5.5	-25.9	Nishio City
A16	137.07	34.87	28.8	6.5	-22.3	Nishio City
A17	137.12	34.89	30.7	8.5	-22.2	Okazaki City
A18	137.08	34.88	29.3	7.9	-21.4	Abe(unpublished)
A19	137.07	34.87	27.3	6.0	-21.3	Nishio City
A20	137.09	34.88	29.0	8.2	-20.8	Abe(unpublished)
A21	137.08	34.87	29.5	9.9	-19.6	Aichi Pref.
A22	137.10	34.86	23.6	5.4	-18.2	Nishio City
A23	137.08	34.88	24.1	8.1	-16.0	Nishio City
A24	137.07	34.87	17.5	5.2	-12.3	Nishio City
A25	137.08	34.85	21.8	10.1	-11.7	Aichi Pref.
A26	137.09	34.83	15.3	4.5	-10.8	Nishio City
A27	137.07	34.87	15.0	4.9	-10.1	Nishio City
A28	137.08	34.88	17.7	8.6	-9.1	Nishio City
A29	137.09	34.88	15.6	8.4	-7.2	Nishio City
A30	137.11	34.89	13.3	8.1	-5.2	Aichi Pref.
A31	137.08	34.88	10.7	6.3	-4.4	Nishio City
A32	137.09	34.85	6.8	7.5	0.7	Aichi Pref.
A33	137.09	34.88	7.3	9.2	1.9	Aichi Pref.
A34	137.08	34.87	7.6	9.7	2.1	Aichi Pref.
B1	137.00	34.67	0.0	-1.7	-1.7	Geological map (National Institute of Advanced Industrial Science and Technology, 2020b)
B2	137.09	34.79	0.0	1.0	1.0	
B3	137.09	34.85	0.0	7.8	7.8	
B4	137.08	34.88	0.0	6.6	6.6	
B5	137.10	34.89	0.0	8.0	8.0	
B6	137.14	34.88	0.0	55.3	55.3	
B7	137.17	34.92	0.0	38.2	38.2	
B8	137.17	35.03	0.0	42.6	42.6	
B9	137.13	35.14	0.0	109.3	109.3	
B10	137.04	35.15	0.0	63.4	63.4	
B11	136.62	35.14	0.0	242.4	242.4	
B12	137.20	34.67	0.0	3.0	3.0	
The data ID with capital A (A1-A34) was derived from the boring data obtained by Aichi Prefecture, Nishio City, Okazaki City and Abe (unpublished).						
The data ID with capital B (B1-B12) was derived from the location of the basement rock represented in the geological map (National Institute of Advanced Industrial Science and Technology, 2020b).						

849

850 Supplementary Table 3. Parameters for the 2D basement model calculated from 10 genetic

851 algorithm (GA) experiments.

Additional Table 3. Parameters for the 2D basement model calculated from 10 GA experiments

ID of GA experiments	Dip of Utsumi Fault (° E)	Dip of Takahama Fault (° W)	Depth Shift of the basement southweset from the Utsumi Fault (m)	Depth Shift of the basement northeast from the Takahama Fault (m)	Rotation of the basement between the Utsumi and Takahama faults (deg to anticlock wise)	Rotation center of between the Utsumi and Takahama faults (km)	Mean absolute error (mgal)	Maximum number of generations
1	72.091	60.665	95.238	18.531	1.035	16.835	0.272	248
2	72.124	65.756	95.221	18.695	1.011	17.086	0.272	313
3	72.108	62.769	95.218	18.757	1.023	16.958	0.272	184
4	72.121	65.018	95.220	18.924	1.013	17.062	0.272	268
5	72.098	61.634	95.221	18.489	1.030	16.887	0.272	222
6	72.124	65.647	95.219	18.710	1.012	17.084	0.272	314
7	72.098	61.547	95.232	18.513	1.030	16.886	0.272	250
8	72.101	61.074	95.315	19.185	1.029	16.892	0.272	155
9	72.098	61.072	95.231	19.024	1.030	16.883	0.272	163
10	72.090	60.577	95.231	18.427	1.036	16.824	0.272	356

852

Figures

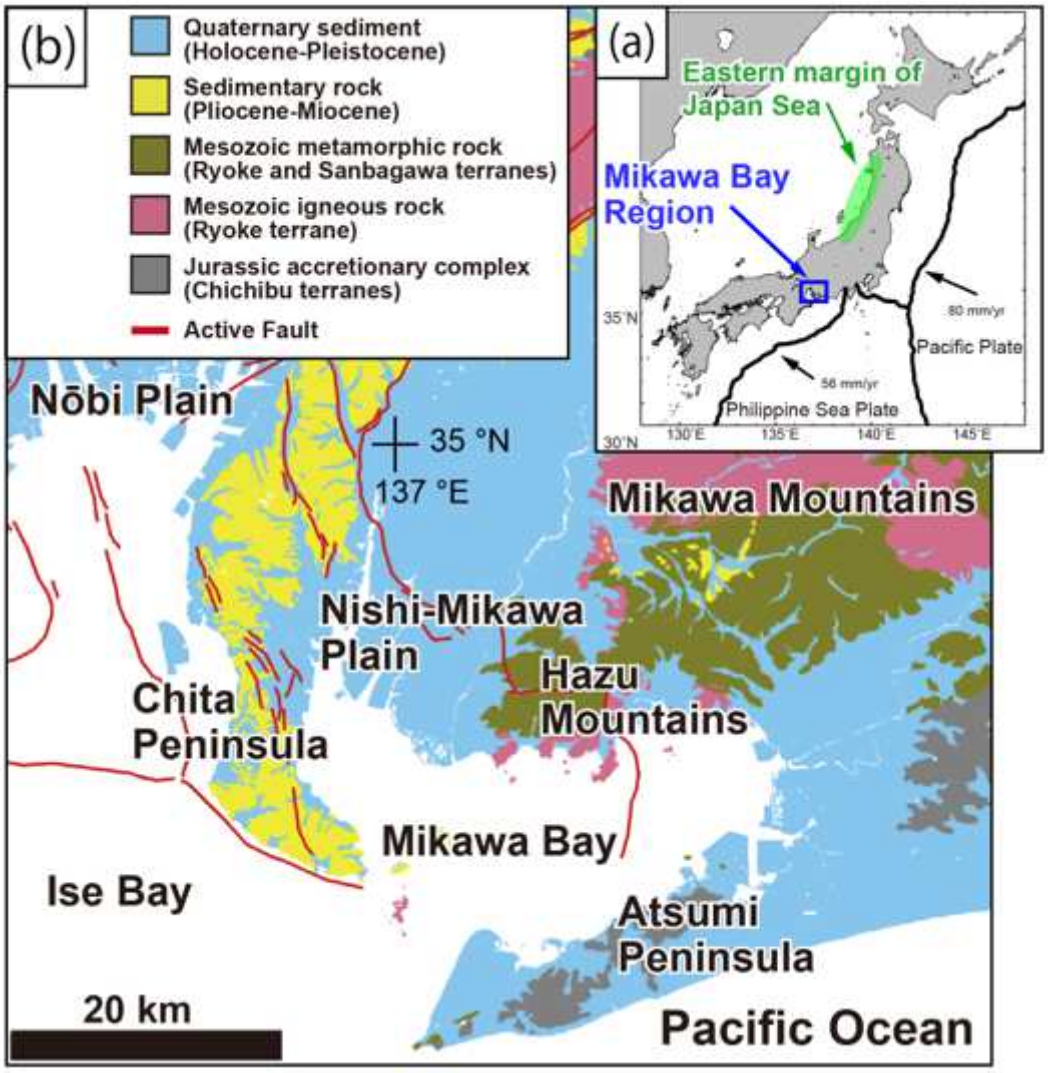

Figure 1

Map showing the tectonic setting of the Japanese islands (a) and the geology of the study area (b) (National Institute of Advanced Industrial Science and Technology 2020b). (a) Thick black lines represent plate boundaries and black arrows represent relative plate motions (after Wei and Seno, 1998). The blue rectangle represents the study area and the green shaded area is the eastern margin of the Japan Sea (see main text for discussion).

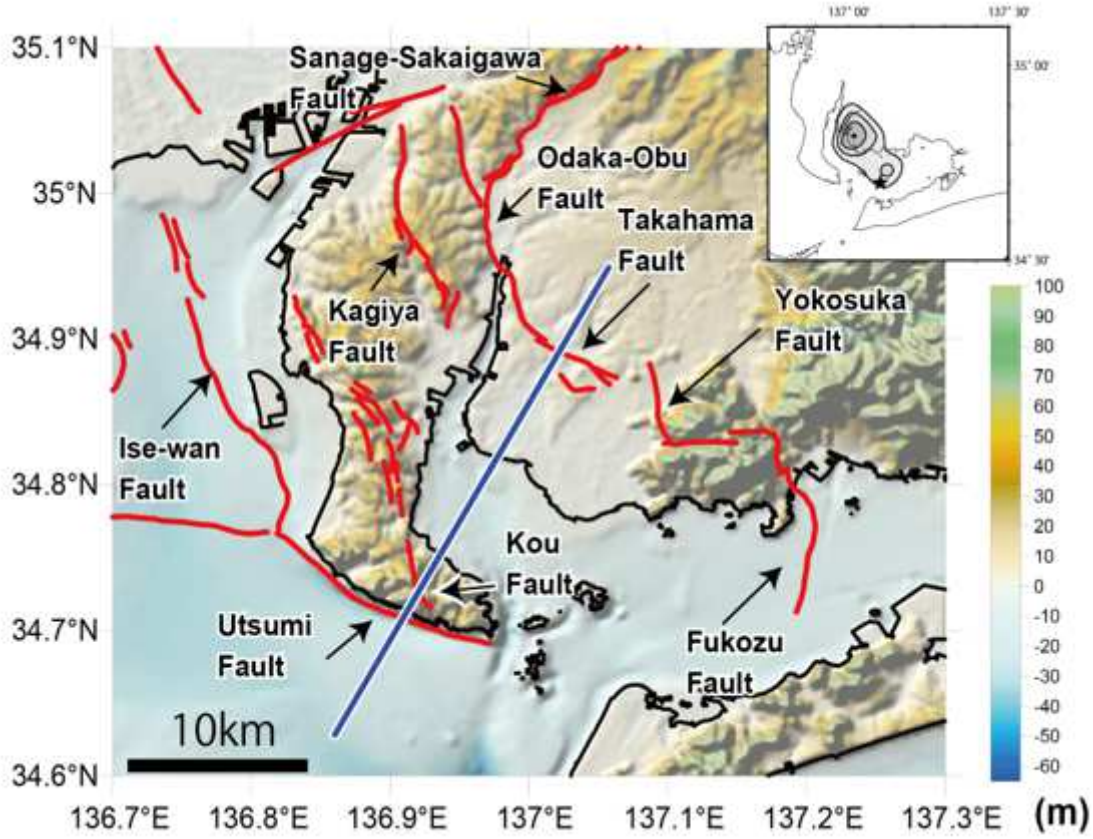

Figure 2

Topography and active faults in the Mikawa Bay Region. Red lines represent the traces of active faults in Figure 1(b) (National Institute of Advanced Industrial Science and Technology, 2020a). The blue line indicates the profile line shown in Figures 8, 9, and 10. The topography is illustrated using the 30 m gridded terrain data compiled by Murata et al. (2018). The top-right panel represents the slip distribution model of the 1945 Mikawa Earthquake (modified after Kikuchi et al., 2003). The increment of contour lines is 0.5 m and the star indicates the epicenter of the 1945 Mikawa Earthquake.

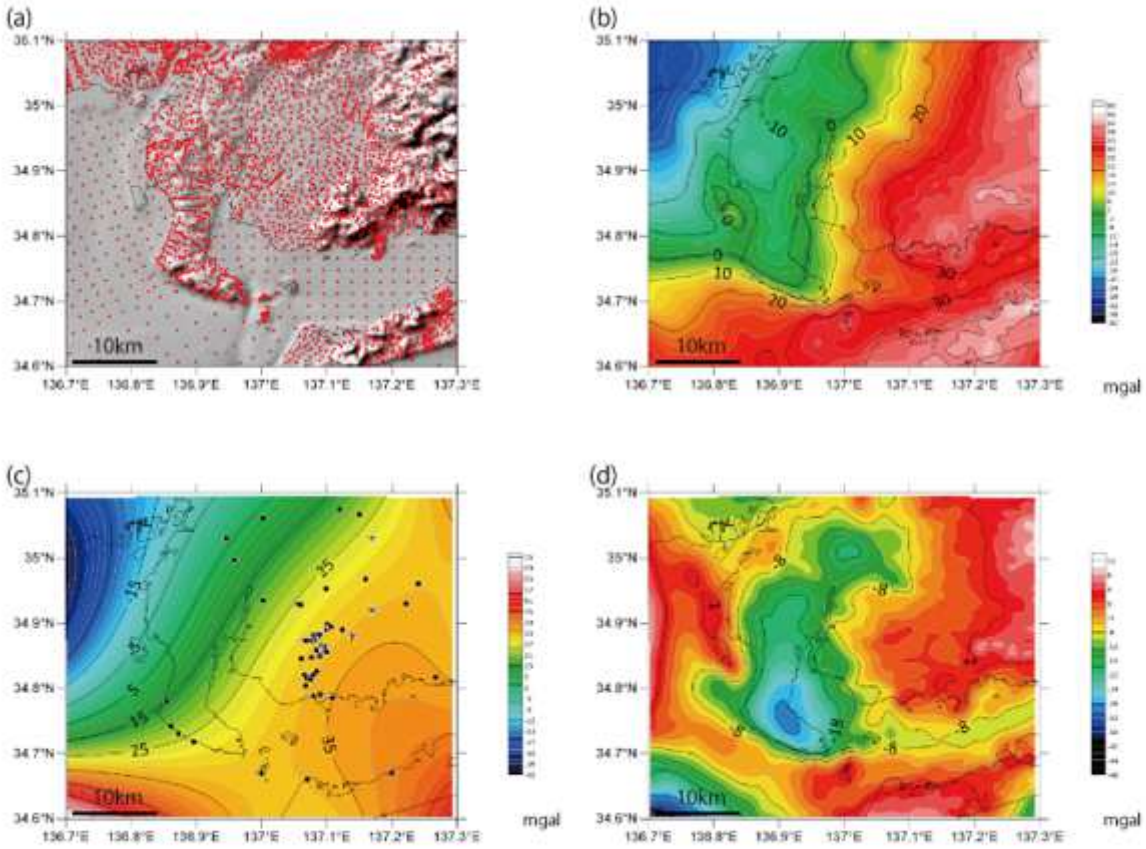

Figure 3

Bouguer anomaly of the study area. (a) Red dots indicate the location of gravity stations used for this analysis. (b) Bouguer anomaly calculated with a reduced density of 2.3 g/cm3. (c) Regional trend of the Bouguer anomaly. Black dots and crosses represent the boring locations and basement exposing locations, respectively. (d) Residual Bouguer anomaly obtained by deducting the regional trend (c) from the original Bouguer anomaly (b). The topography (a) is illustrated by using the 30 m gridded terrain data compiled by Murata et al. (2018).

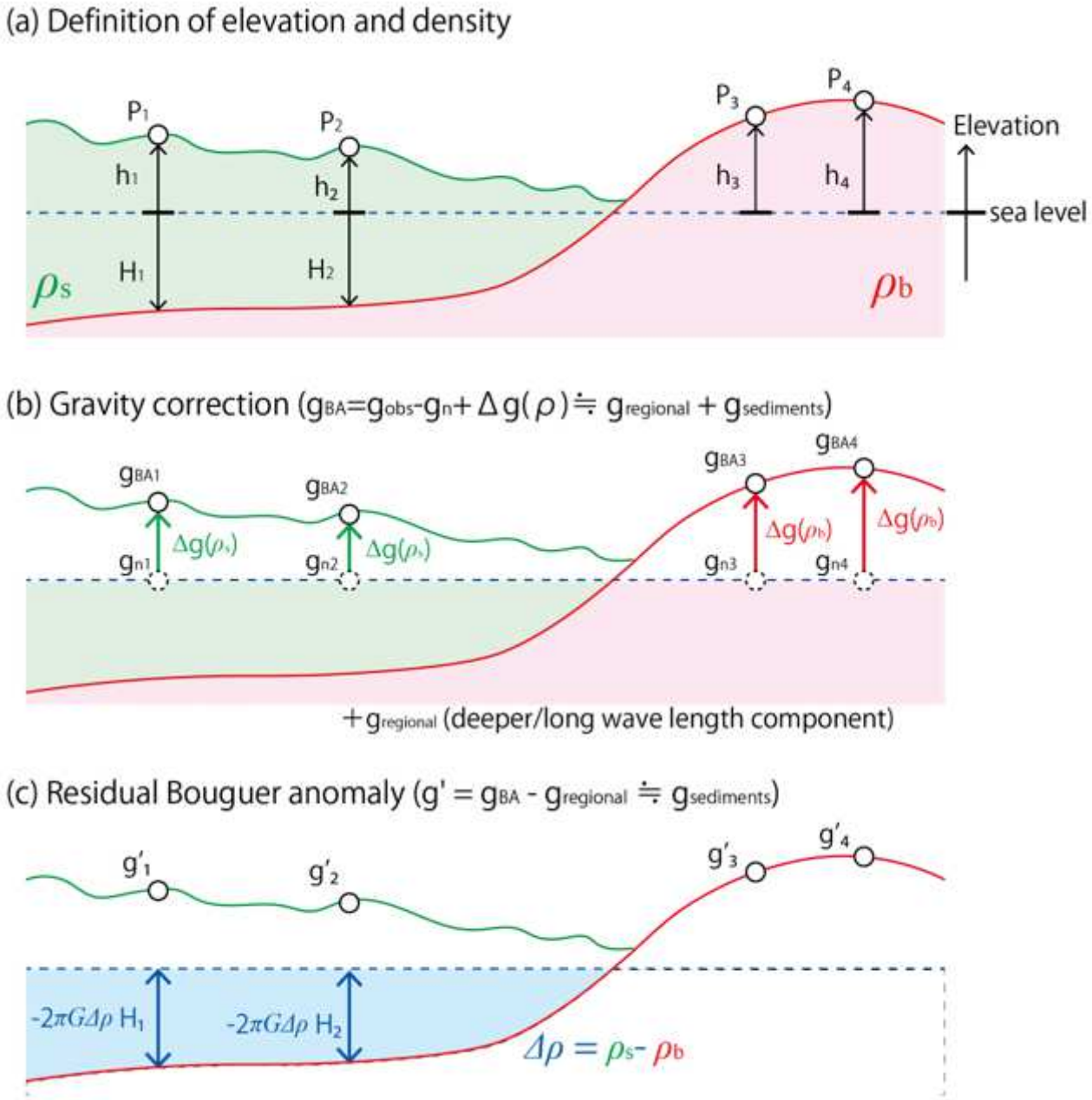

Figure 4

Schematic diagrams showing the calculation of residual Bouguer anomalies at the boring sites and basement exposure points. (a) Definition of the elevation of points (h) and the density of the basement (ρb) and one unit of sediments/sedimentary rocks (ρs). The elevation of the buried basement surface is represented by H. (b) Gravitational corrections ( ) (Bouguer, free-air and terrain correction) are calculated using the density of the rock exposed at the observation points. gn is normal gravity in accordance with the Geodetic Reference System 1980 (GRS80). The corrected Bouguer anomaly (gBA) represents the Bouguer anomaly considered. (c) The residual Bouguer anomaly (g') is obtained by removing the regional trend from the Bouguer anomaly (gBA). The residual Bouguer anomaly must consist of the gravity

anomaly from the thickness of the sediments/sedimentary rocks (i.e., the elevation of the basement surface).

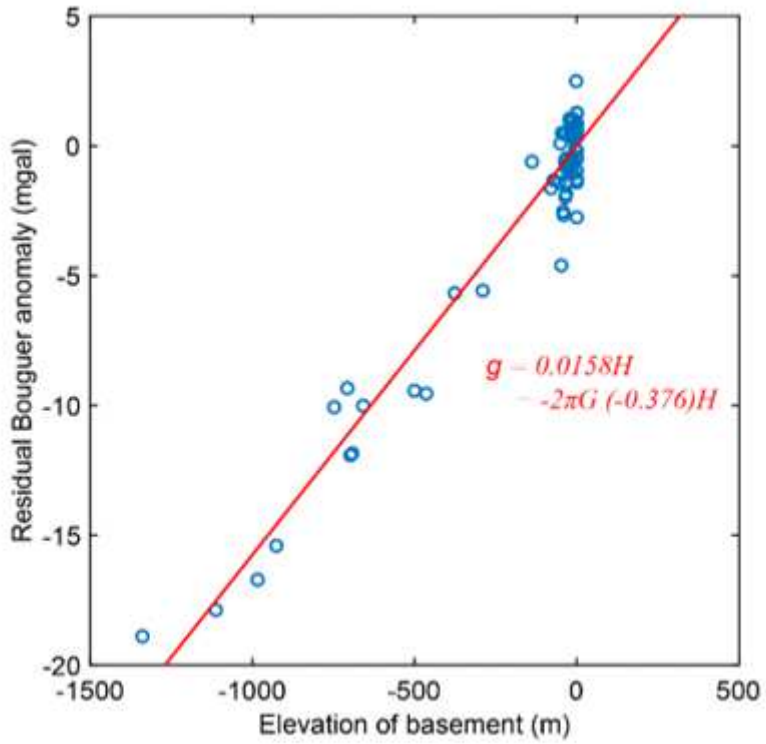

Figure 5

Relationship between the elevation of the basement and the residual Bouguer anomaly at the boring site or basement exposure (Fig. 4). The red line represents the relationship between the elevation of the basement and the residual Bouguer anomaly by using the least square method.

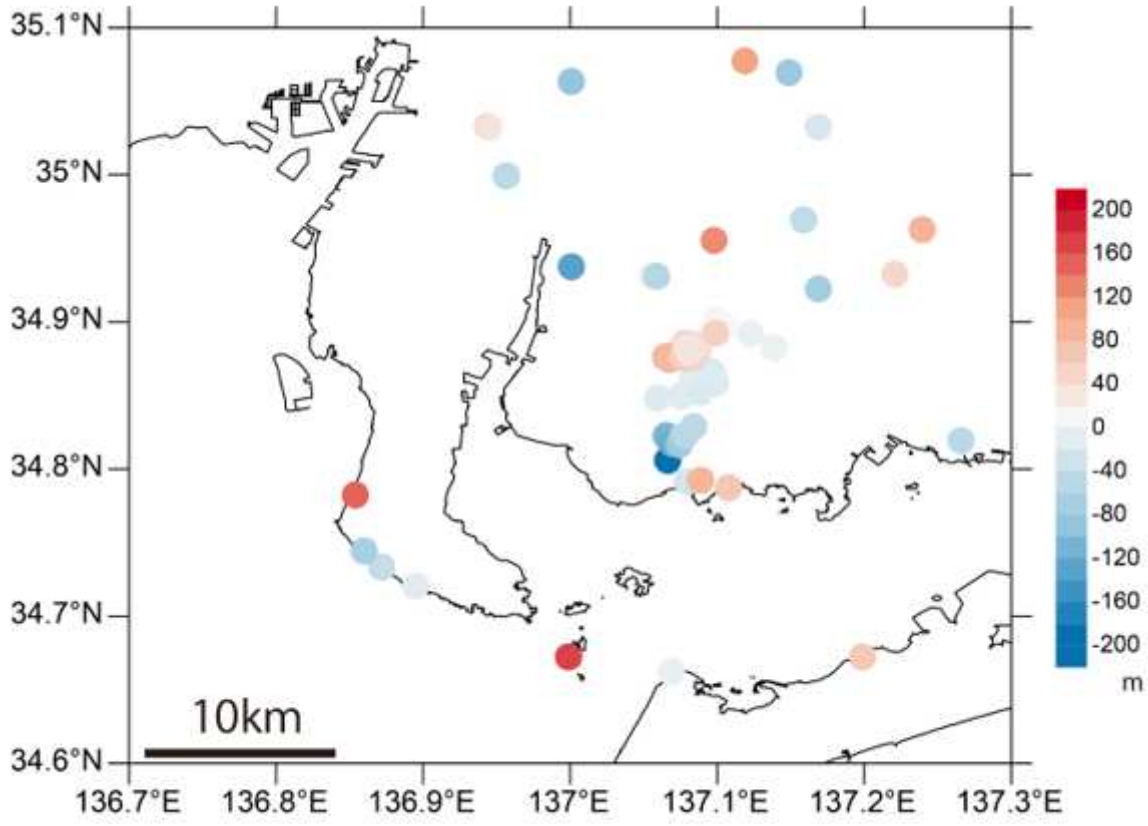

Figure 6

Difference between the observed elevation of the basement surface and the calculated elevation of the basement surface (see Fig. 5).

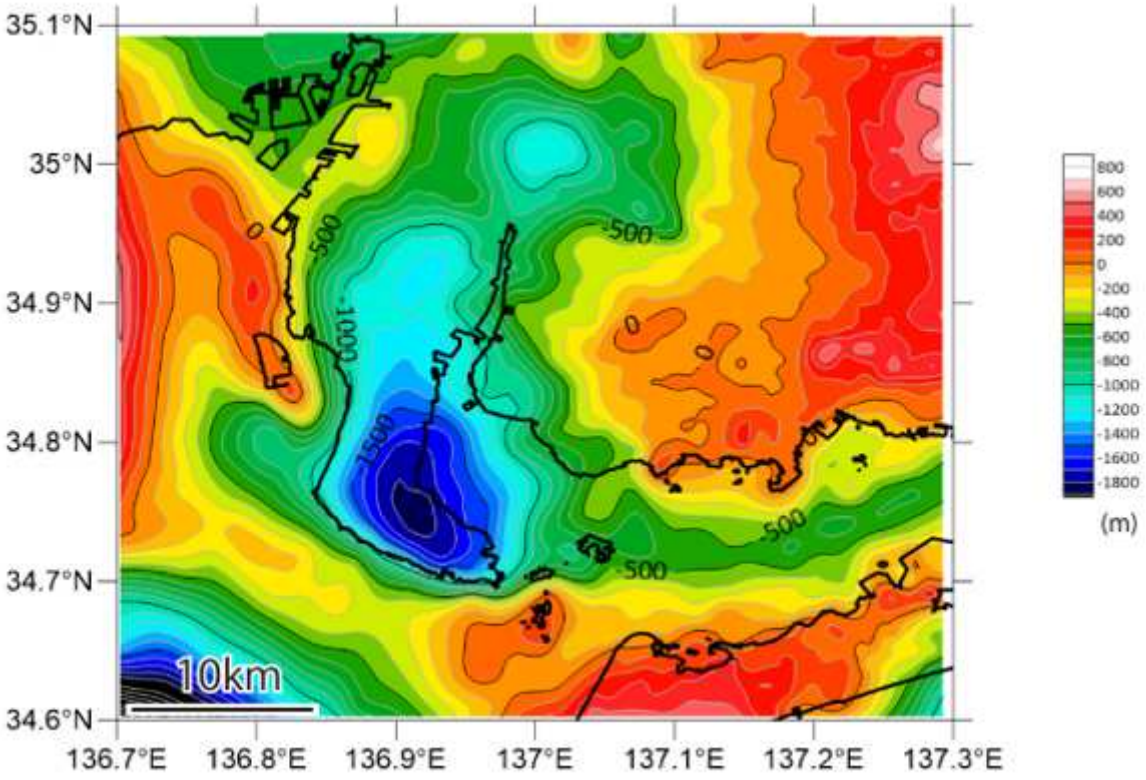

Figure 7

Gravity basement map obtained using the relationship between the depth of the basement and the residual Bouguer anomaly (Fig. 5) based on the the residual Bouguer anomaly map (Fig. 3d).

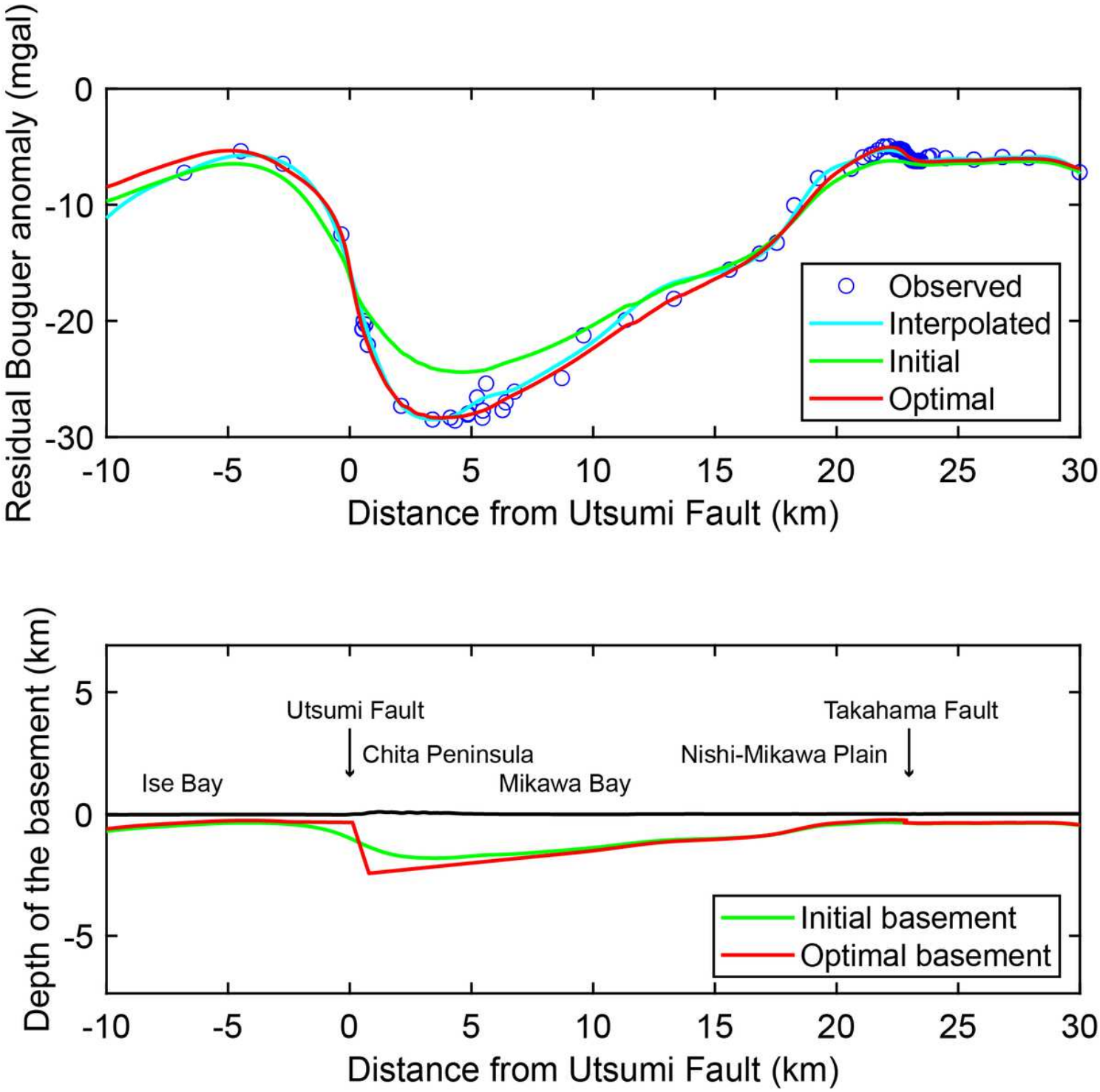

Figure 8

Profiles of the Bouguer anomaly (a) and the topography of the basement surface (b). (a) The observed and interpolated residual Bouguer anomalies are represented by the open circles and cyan line, respectively. The interpolated residual Bouguer anomalies come from that of the Fig. 3 (d). The green line and red line represent the calculated Bouguer anomaly from the initial model (green in b) and the optimum model (red in b) using the 2D Talwani's method. (b) The green line represents the initial model extracted from the gravity basement model (Fig. 5) along the survey line. The red line represents the

optimum basement model obtained by selecting the best parameters (see Table 2). The black line represents the elevation of the ground surface. The origin of the x-axis is set as the tip of the Utsumi Fault in both a and b.

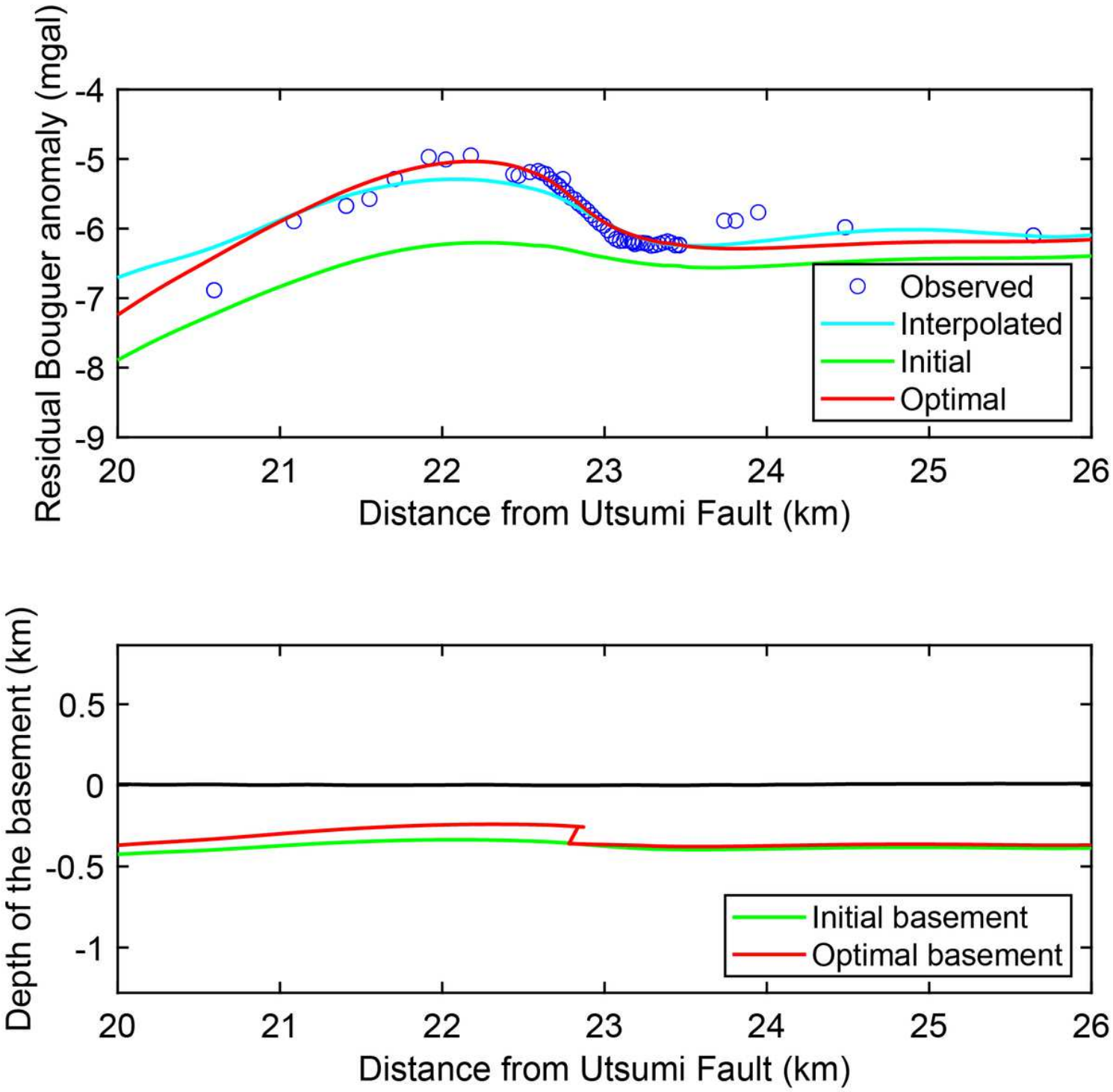

Figure 9

Close-up views of the profiles of the Bouguer anomaly (a) and the topography of the basement surface (b) around the Takahama Fault. The tip of the Takahama Fault is located at 22.98 km. (a) The observed and interpolated residual Bouguer anomalies are represented by open circles and the cyan line, respectively. The interpolated residual Bouguer anomalies come from that of the Fig. 3 (d). The green line

and red line represent the calculated Bouguer anomaly from the initial model (green in b) and the optimum model (red in b) using the 2D Talwani's method. (b) The green line represents the initial model extracted from the gravity basement model (Fig. 5) along the survey line. The red line represents the optimum basement model obtained by selecting the best parameters (Table 2). The black line represents the elevation of the ground surface. The origin of the x-axis is set at the tip of the Utsumi Fault in both a and b.

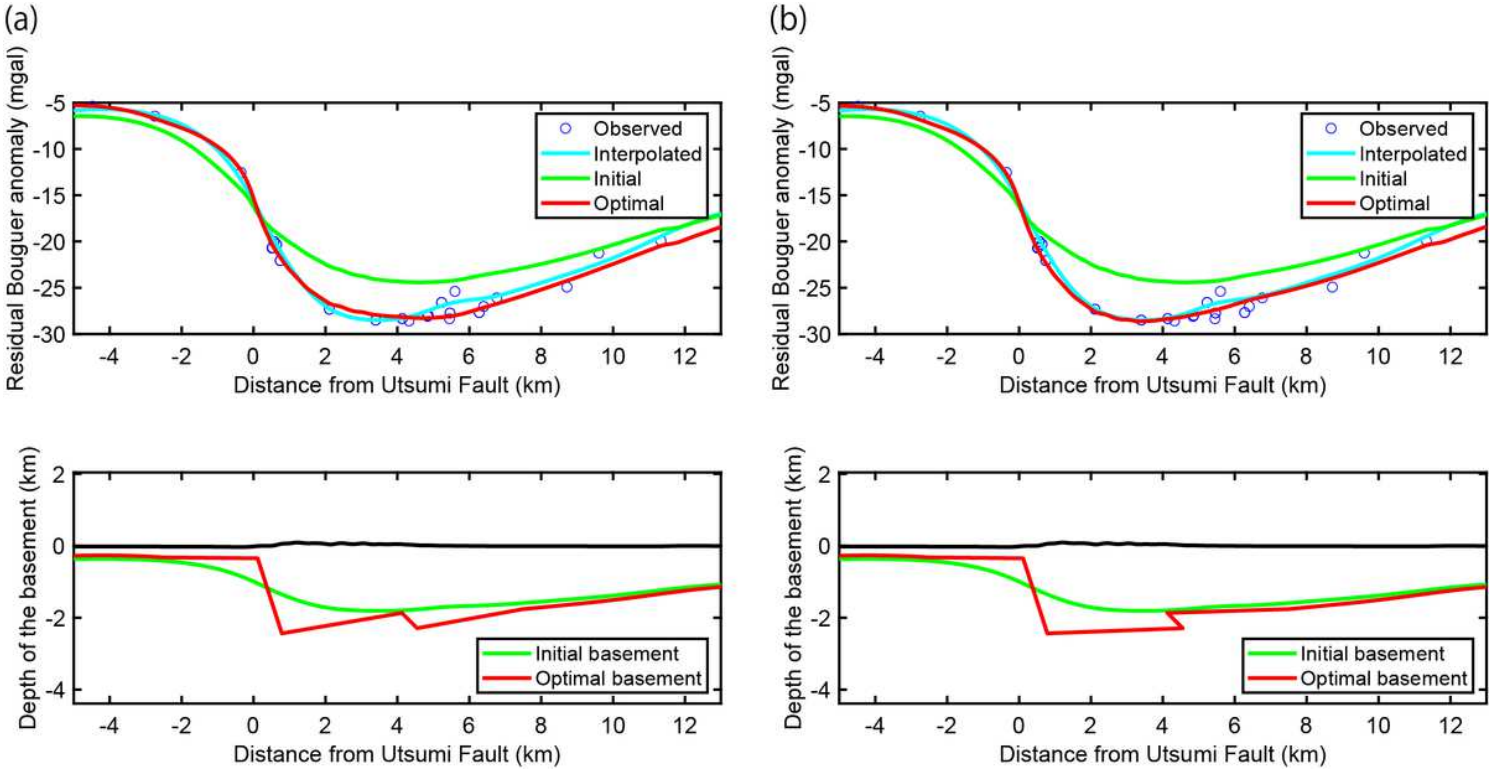

Figure 10

Profiles of the Bouguer anomaly and the topography of the basement surface with 600 m of displacement along the Kou Fault at 2.26 km with a dip of 45°E. (a) Reverse fault structure of the Kou Fault using the optimal basement model. (b) Normal fault structure of the Kou Fault using the optimal basement model. Lines and circles are same as shown in Figure 8. The origin of the x-axis is set at the tip of the Utsumi Fault in both a and b.

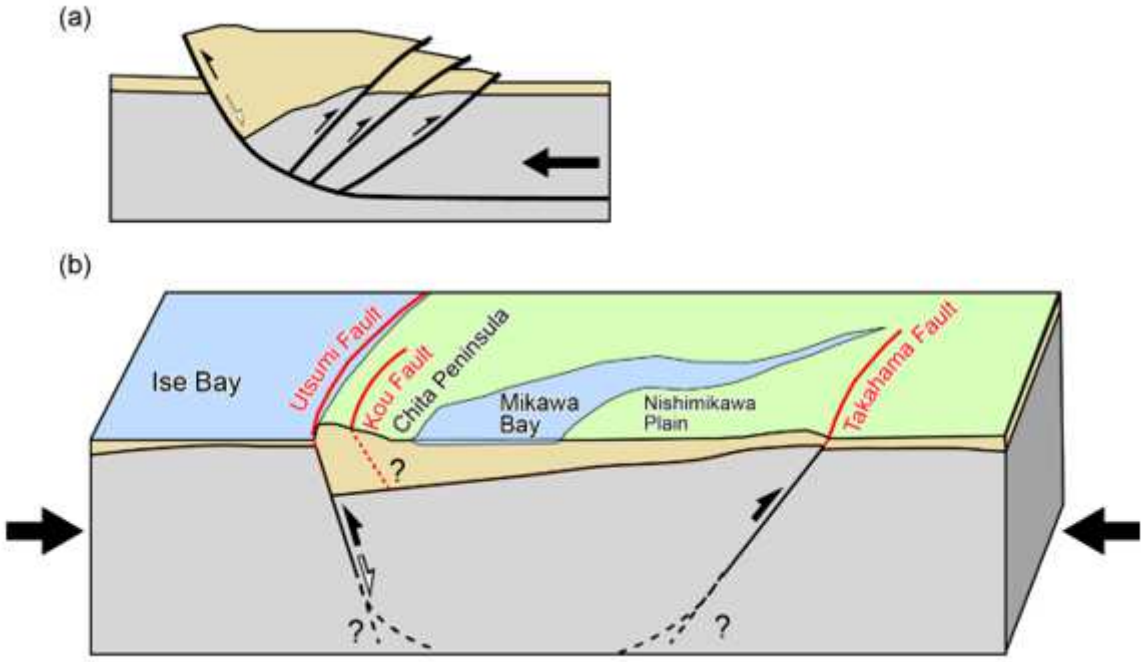

Figure 11

(a) Conceptual models for thrust faults developed by the dip-slip inversion of a normal fault system (modified after McClay and Buchanan, 1992). The white arrow represents normal faulting during the extensional stage. Black arrows indicate reverse faulting during the compressional stage following the extensional stage. (b) Conceptual models for the fault system across the Chita Peninsula and the Nishi–Mikawa Plain (not to scale). The white arrow represents the normal faulting in the extensional stage in Miocene. Black arrows indicate reverse faulting during the compressional stage following extensional stage in the Pliocene to Quaternary.

Supplementary Files

This is a list of supplementary files associated with this preprint. Click to download.

- Table1.png
- Table2BestFitParameters200910.xlsx
- 00GraohicAbstract200516.png
- SupFigure12MiyakawaetalPEPS2020r3.docx
- SupTable1GravityObs200515.xlsx
- SupTable2BasementDepth200909r.xlsx
- SupTable3OptimizationResults200910.xlsx